UPPSALA
UNIVERSITET

Digital Comprehensive Summaries of Uppsala Dissertations from the Faculty of Science and Technology 1746

Design of Rare Earth Free Permanent Magnet Generators

PETTER EKLUND

ACTA
UNIVERSITATIS
UPSALIENSIS
UPPSALA
2018

ISSN 1651-6214
ISBN 978-91-513-0510-3
urn:nbn:se:uu:diva-366344

Dissertation presented at Uppsala University to be publicly examined in Polhemsalen, Ångströmlaboratoriet, Lägerhyddsvägen 1, Uppsala, Friday, 18 January 2019 at 09:15 for the degree of Doctor of Philosophy. The examination will be conducted in English. Faculty examiner: Docent Oskar Wallmark (KTH, Elkraftteknik).

Abstract
Eklund, P. 2018. Design of Rare Earth Free Permanent Magnet Generators. *Digital Comprehensive Summaries of Uppsala Dissertations from the Faculty of Science and Technology* 1746. 75 pp. Uppsala: Acta Universitatis Upsaliensis. ISBN 978-91-513-0510-3.

Low speed permanent magnet (PM) synchronous generators (SGs) are commonly used in renewable energy. Rare earth (RE) PMs such as neodymium-iron-boron are a popular choice due to their high performance. In 2011 supply and cost issues were added to the previously existing environmental concerns regarding REPM raw materials as the world's major producer China imposed export restrictions. This thesis aims to investigate and propose design solutions for PMSGs that do not use REPMs. Two approaches are used: to design generators using the cheaper and more abundant ferrite PM materials, and to investigate how properties of new PM materials influence SG design.

A ferrite PM rotor is designed to replace a REPM rotor in an experimental 12 kW wind power generator. The new design employs a flux concentrating spoke type rotor to achieve performance similar to the old REPM rotor while using ferrite PMs. The ferrite PM rotor design is built. The air gap length, magnetic flux density in the air gap, PM remanence, and voltage at both load and no load are measured. The generator has lower no load voltage than expected, which is mainly explained by lower than specified remanence of the ferrite PMs in the prototype. With the measured remanence inserted into the calculations some discrepancy remains. It is found that the discrepancy can be explained by the magnetic leakage flux in the end regions of the spoke type rotor, which is not modeled in the two dimensional simulations used for the design calculations.

To investigate the influence of PM material properties three different PM rotor topologies are optimized for torque production using PM materials described by their remanence, recoil permeability, and demagnetization resistance. Demagnetization is considered using currents determined by a novel, winding design independent short circuit model. It is found that the spoke type rotor gives the highest torque of the three rotor topologies for low remanence materials as long as the PMs have sufficient demagnetization resistance. For high remanence materials the surface mounted PM rotor can give higher torque if the demagnetization resistance is high, but otherwise a capped PM rotor gives higher torque.

Keywords: permanent magnet generators, electrical machine design, ferrite permanent magnet

Petter Eklund, Department of Engineering Sciences, Electricity, Box 534, Uppsala University, SE-75121 Uppsala, Sweden.

ISSN 1651-6214
ISBN 978-91-513-0510-3
urn:nbn:se:uu:diva-366344 (http://urn.kb.se/resolve?urn=urn:nbn:se:uu:diva-366344)

Till mor och far
samt min älskade Valdis

"Reality is that which, when you stop believing in it, doesn't go away."
Philip K. Dick

List of papers

This thesis is based on the following papers, which are referred to in the text by their Roman numerals.

I **P. Eklund**, S. Sjökvist, S. Eriksson, M. Leijon, "A Complete Design of a Rare Earth Metal-Free Permanent Magnet Generator," *Machines*, vol. 2, issue 2, pp. 120–133, May 2014.

II **P. Eklund**, S. Eriksson, "Air Gap Magnetic Flux Density Variations due to Manufacturing Tolerances in a Permanent Magnet Synchronous Generator," in the proceedings of *XXII International Conference on Electrical Machines,* pp. 93–99, Lausanne, Switzerland, September 4–7, 2016.

III **P. Eklund**, S. Eriksson, "Winding Design Independent Calculation Method for Short Circuit Currents in Permanent Magnet Synchronous Machines," in the proceedings of *XXIII International Conference on Electrical Machines,* pp. 1021–1027, Alexandroupoli, Greece, September 3–6, 2018.

IV **P. Eklund**, S. Eriksson, "The influence of permanent magnet material properties on generator rotor design," submitted to *IET Electric Power Applications*, 2 May 2018.

V **P. Eklund**, J. Sjölund, M. Berg, S. Eriksson, M. Leijon, "Experimental Evaluation of a Rare Earth-Free Permanent Magnet Generator," submitted to *IEEE Transactions on Energy Conversion*, 11 October 2018.

VI D. Elamalayil Soman, J. Loncarski, L. Gerdin, **P. Eklund**, S. Eriksson, and M. Leijon, "Development of Power Electronics Based Test Platform for Characterization and Testing of Magnetocaloric Materials," *Advances in Electrical Engineering,* vol. 2015, Article ID 670624, 7 pages, 2015.

VII S. Sjökvist, **P. Eklund**, S. Eriksson, "Determining demagnetisation risk for two PM wind power generators with different PM material and identical stators," *IET Electric Power Applications,* vol. 10, issue 7, pp. 593–597 2016.

VIII **P. Eklund**, J. Sjölund, S. Eriksson, M. Leijon, "Magnetic End Leakage Flux in a Spoke Type Rotor Permanent Magnet Synchronous Generator," contribution to *19th International Conference on Electrical Machines and Drives,* Madrid, Spain, March 26–27, 2017. (Unreviewed conference paper.)

Reprints were made with permission from the publishers.

Contents

1 Introduction 13
1.1 A Short history of Permanent Magnet Machines and Permanent Magnet Materials 14
1.2 Related Projects at Uppsala University 15
1.2.1 Wind Power Research at the Division of Electricity 15
1.2.2 Electrical Machine Design at the Division of Electricity 16
1.2.3 Development of Novel Permanent Magnet Materials 16
1.3 Overview of Electrical Machine Design Research 17
1.4 Aim of the Thesis 18
1.5 Outline of the Thesis 19

2 Theory 20
2.1 Electromagnetism and Rotating Electrical Machines 20
2.1.1 The Generator Equation 21
2.1.2 Magnetic Force and Torque 23
2.2 Magnetic Materials 24
2.3 The Park Transform 26
2.4 The Finite Element Method 27
2.5 Potential Formulations of Maxwell's Equations 27
2.5.1 Vector Potential Formulation 28
2.5.2 Scalar Potential Formulation 29

3 Method 30
3.1 Finite Element Method Simulations of Electrical Machines 30
3.2 Mechanical Modeling 31
3.3 Magnetic and Mechanical Air Gap Measurements 32
3.4 End Region Magnetic Flux Density Measurements 34
3.5 Load and No Load Experiments on the Generator with Ferrite Permanent Magnet Rotor 34
3.6 Winding Design Independent Short Circuit Current Calculation 35
3.6.1 Definition of Quantities 35
3.6.2 The Short Circuit Model 37
3.6.3 Validation 37
3.7 Rotor Topologies for Different Permanent Magnet Material Parameters 38

4 Design and Testing of a Rare Earth Free Permanent Magnet Rotor 41
4.1 Electromagnetic Design Process 41
4.2 Mechanical Design Process 42
4.3 Predicted Electromagnetic Performance 44
4.4 Experiences from Building the Design — Discussion 47
4.5 Experimental Results and Discussion 48
4.5.1 Manufacturing Tolerances and Air Gap Magnetic Flux Density 48
4.5.2 Experimental Verification of Simulations and End Effects 50

5 Electrical Machine Design for Parametrized Permanent Magnet Materials — Results and Discussion 53
5.1 Validation of Winding Design Independent Short Circuit Current Calculation 53
5.2 Permanent Magnet Rotor Topology Comparison 53

6 Conclusions 59

7 Future Work 61

8 Summary of Papers 62

9 Svensk sammanfattning 66

10 Acknowledgments 68

References 70

List of Acronyms

2D Two dimensional
3D Three dimensional
BC Boundary condition
DC Direct current
dq0 Direct-quadrature-zero-axis
EMF Electromotive force
FEM Finite element method
IPM Interior permanent magnet, a class of PM rotor
MMF Magnetomotive force
NdFeB Neodymium-iron-boron, a PM material
ODE Ordinary differential equation, a differential equation with a single independent variable
PDE Partial differential equation, a differential equation with multiple independent variables
PM Permanent magnet
PMSG Permanent magnet synchronous generator
RE Rare earth, a group of elements in the periodic table of elements
RMS Root mean square
SG Synchronous generator
SM Synchronous machine
SmCo Samarium-cobalt, a PM material
VAWT Vertical axis wind turbine

List of Symbols (Latin)

Symbol	Description	Unit
$\boldsymbol{A}$	Magnetic vector potential	Tm
A_{eff}	Effective cross section area of winding	m^2
A_z	Magnetic vector potential, axial component	Tm
$\boldsymbol{B}$	Magnetic flux density	T
B	Magnetic flux density, component in direction given by subscript, or magnitude	T
B_δ	Measured air gap magnetic flux density	T
$B_{\delta,\rho}$	Magnetic flux density in the air gap, radial component	T
$\hat{B}^h_{\delta,\rho}$	Amplitude of the hth harmonic component of $B_{\delta,\rho}$	T
$\check{B}^h_{\delta,\rho}$	Phase of the hth harmonic component of $B_{\delta,\rho}$	rad
$B_{\text{free PM}}$	Magnetic flux density of a free lying PM	T
$\lvert BH\rvert_{\max}$	Maximum energy product, a PM figure of merit	J/m^3
B_{r}	Remanent magnetic flux density	T
c	Number of parallel circuits	1
$C_{B^{\min}_{\text{PM}}}$	Demagnetization parameter, gives the fraction of B_{r} which is the lowest allowed magnetic flux density along magnetization	1
D_{si}	Stator inner diameter	m
$\text{d}\boldsymbol{l}$	A directed line segment	m
$\text{d}\boldsymbol{S}$	A surface element with a unit normal	m^2
∂S	The right-hand oriented boundary of a surface S	–
$\boldsymbol{E}$	Electric field	V/m
E	Electric field, component in direction given by subscript, or magnitude	V/m
$\mathscr{E}$	Electromotive force	V
$\mathscr{E}_{\text{turn}}$	Electromotive force per turn	V
$\mathscr{E}_{\text{turn},h}$	Electromotive force per turn of harmonic order h	V
$\mathscr{E}^h_{\text{RMS}}$	Electromotive force of harmonic order h of a winding, RMS value	V
$\boldsymbol{F}$	Force	N
$\mathscr{F}_d$	Direct axis MMF	A
f_{el}	Electrical frequency	Hz
$\mathscr{F}_q$	Quadrature axis MMF	A
$\boldsymbol{H}$	Magnetizing field	A/m
h	Harmonic order	1
H	Magnetizing field, component in direction given by subscript, or magnitude	A/m
H_c	Coercivity (also normal coercivity)	A/m
H^i_c	Intrinsic coercivity	A/m
h_{PM}	Height (along magnetization) of permanent magnet	m
i_0	Zero axis current	A
i_a	Current in phase a	A
i_b	Current in phase b	A
i_c	Current in phase c	A

Continued on next page

Symbol	Description	Unit
i_d	Direct axis current	A
i_q	Quadrature axis current	A
i_a^Δ	Maximum error in i_a, additional subscript indicates sampling at the instant given by the subscript	A
i_c^Δ	Maximum error in i_c, additional subscript indicates sampling at the instant given by the subscript	A
$\boldsymbol{J}$	Electric current density	$\mathrm{A/m^2}$
J_z	Electric current density, axial component	$\mathrm{A/m^2}$
$\hat{J}_{z,d}$	Direct axis current density amplitude	$\mathrm{A/m^2}$
$\hat{J}_{z,q}$	Quadrature axis current density amplitude	$\mathrm{A/m^2}$
$k_{d,h}$	Winding distribution factor for harmonic order h	1
$k_{p,h}$	Winding pitch factor for harmonic order h	1
$k_{w,h}$	Winding factor for harmonic order h	1
l_{act}	Active length of the machine	m
L_d	Direct axis synchronous inductance	H
L_q	Quadrature axis synchronous inductance	H
$\boldsymbol{M}$	Magnetization	$\mathrm{Am^2/m^3}$
M	Magnetization, component in direction given by subscript, or magnitude	$\mathrm{Am^2/m^3}$
m	Number of phases (typically three)	1
M_s	Saturation magnetization	$\mathrm{Am^2/m^3}$
N	Number of samples	1
n_s	Number of turns per slot	1
P	Power, instantaneous if written as function of t, sampled at instant indicated by subscript, or mean	W
p	Number of poles	1
P^Δ	Maximum error of mean power	W
q	Number of slots per pole and phase	1
q_e	Electric charge	C
R_{s}	Resistance of one stator phase winding	Ω
S	A bounded surface with boundary ∂S	–
t	Time	s
T_{em}	Electromagnetic torque	Nm
$\boldsymbol{v}$	Velocity	m/s
v_{ab}	Voltage between phase a and b, additional subscript indicates sampling at the instant given by the subscript	V
v_{bc}	Voltage between phase b and c, additional subscript indicates sampling at the instant given by the subscript	V
v_d	Direct axis terminal voltage	V
v_q	Quadrature axis terminal voltage	V
v_{ab}^Δ	Maximum error in v_{ab}, additional subscript indicates sampling at the instant given by the subscript	V
v_{bc}^Δ	Maximum error in v_{bc}, additional subscript indicates sampling at the instant given by the subscript	V
x	A signal, addition of subscript indicates sampling at the instant given by the subscript	1

Continued on next page

Symbol	Description	Unit
x^{Δ}	The measurement error in a signal x, subscript indicates sampling at the instant given by the subscript	1
X_{RMS}	The RMS value of a signal x	1
$X_{\mathrm{RMS}}^{\Delta}$	The maximum error of the RMS value of a signal x	1
z	Axial coordinate	m

List of Symbols (Non-Latin)

Symbol	Description	Unit
α_{turn}	Angular location of a turn	rad
δ	Air gap length	m
δ_{ij}	Kronecker delta function, equals one for equal indices and zero otherwise	1
ε_0	Permittivity of free space	$\mathrm{As/Vm}$
$\theta_{\mathrm{rot}}^{\mathrm{el}}$	Electrical rotor angle	rad
Λ_d	Direct axis permeance per unit length	$\mathrm{H/m}$
Λ_q	Quadrature axis permeance per unit length	$\mathrm{H/m}$
μ_0	Permeability of free space	$\mathrm{Vs/Am}$
μ_{r}	Relative permeability	1
μ_{rec}	Relative recoil permeability	1
ρ	Radial distance coordinate (cylindrical system)	m
ρ_{e}	Electric charge density	$\mathrm{C/m^3}$
ρ_{el}	Resistivity of material	$\Omega\mathrm{m}$
ϱ_{s}	Resistance per unit length of winding as seen from the magnetic circuit	Ω/m
$\boldsymbol{\sigma}$	Maxwell stress tensor	Pa
σ_{ij}	Maxwell stress tensor, i-direction component on surface with negative-j-direction normal	Pa
τ_c	Mechanical coil pitch angle	rad
ϕ_m	Magnetic scalar potential	A
φ	Azimuthal coordinate (cylindrical system)	rad
φ_{el}	Electrical azimuthal coordinate in rotor reference frame	rad
Φ_d	Magnetic flux per unit length linking to the direct axis	$\mathrm{Wb/m}$
Φ_{PM}	Magnetic flux per unit length due to the PMs linking to the direct axis	$\mathrm{Wb/m}$
Φ_q	Magnetic flux per unit length linking to the quadrature axis	$\mathrm{Wb/m}$
ψ_F	Magnetic flux linkage from the field structure	Wb
Ω	Mechanical speed of rotation	$\mathrm{rad/s}$
ω_{el}	Electrical angular frequency	$\mathrm{rad/s}$
$\boldsymbol{\nabla}$	Nabla operator, a spatial differentiation operator used for the gradient ($\boldsymbol{\nabla}$), divergence ($\boldsymbol{\nabla}\cdot$), or rotation ($\boldsymbol{\nabla}\times$) of a vector field	$1/\mathrm{m}$
∇^2	Laplace operator, a second order spatial differentiation operator	$1/\mathrm{m^2}$

1. Introduction

It is hard to imagine modern society without electric power. Electric power provides light, heat for cooking and residential heating, drives a wide range of machinery and appliances, and powers all kinds of electronic devices. The majority of the energy converted into electric power is done so by the use of rotating electrical machines. In most large power stations the rotating electrical machine is a synchronous generator (SG) driven by either a steam turbine or water turbine. There are some other types of devices that are used for large scale generation of electric power. One is the induction generator, a different kind of rotating electrical machine, which is sometimes used in small scale hydropower and in wind power. Another is the photovoltaic cell, a solid-state electrical device that converts the energy in light into electrical energy.

The simplest possible description of a SG is a rotating magnet surrounded by coils of conductive material. The alternating magnetic flux density caused by the spinning magnet induces an electric field which can perform work on the charge carriers in the coils. There are two options for the rotating magnet of the SG: an electromagnet or a permanent magnet (PM). In large power stations, where the generator is directly connected to the grid, the electromagnet is usually chosen as it allows the output voltage and reactive power output of the SG to be controlled. Using a PM can be an option when it is desirable to avoid the losses in the winding of the electromagnet or when a less complex machine is desirable [1]. One application where PMs are popular in SGs is wind power [2].

Since the invention of the neodymium-iron-boron (NdFeB) PM in the 1980s it has been a popular PM material for use in electrical machines [3]. In 2011, however, the world market price of the minerals needed for the manufacture of NdFeB PMs soared due to export restrictions imposed by the Chinese government [2, 4]. As China has a majority share of the world production of these minerals it was made apparent that dependence on NdFeB was both a financial and strategical risk. In response to this risk and environmental concerns there has been research on both new PM materials and decreased dependence on NdFeB, either by using less or substituting it entirely. This thesis falls into the last of these options, investigating how to make the best use of both existing alternatives, e.g. ferrite PMs, and anticipating the emergence of new PM materials by studying how different PM material properties impact design of PM machine design. The study of how PM material properties affect PM machine design may be able to provide some guidance to those pursuing the first option.

1.1 A Short history of Permanent Magnet Machines and Permanent Magnet Materials

The following section has previously appeared in the author's licentiate thesis [5].

Permanent magnets have been known since antiquity, in the form of naturally occurring magnetized magnetite; an iron oxide. It was also known that a piece of iron could be magnetized by touching or rubbing it with a magnet. Ørsted's discovery that electric currents cause magnetic fields in 1825, and the invention of the electromagnet, started research in electrical motors. With Faraday's discovery of induction in 1831 it was realized that also the opposite of a motor was possible. The first reported generator, designed and built by Hippolyte Pixii in 1832, used a PM. In 1856 Werner Siemens became the first to place the windings in slots; a concept that still dominates electric machine design. During the last two decades of the nineteenth century the three phase system, with electrically excited synchronous generators and motors, emerged. [6]

During the early twentieth century there were some improvements in magnetically hard steels, and by the early 1930s the first alnico PM materials are patented [7]. Since they are metallic they can be used as structural parts of the rotor which allows designs with integrally cast PM rotors. There are also suggestions for designs with alnico poles bolted to a magnetically soft spindle. Alnico is sensitive to demagnetization and therefore require both stabilization and some consideration in the magnetic circuit design [8].

The next major PM material to be introduced was the hard ferrite which was introduced in the early 1950s [9]. While it has lower performance than alnico it is more resistant to demagnetization. One early design, suggested for use with either the new ferrite or alnico is the claw pole rotor described in [10]. A spoke type PM rotor is also mentioned as suitable for use with ferrites in [1].

In 1969 a method of manufacturing samarium-cobalt (SmCo) PMs was published. This was the first of the high energy rare earth (RE) permanent magnets [11]. Although SmCo PMs have very high energy density and excellent temperature stability they are mechanically fragile and require a rotor design that provides the PM with mechanical support [12]. Further, both samarium and cobalt are expensive metals.

The next major step in the rare earth PM development was the neodymium-iron-boron (NdFeB) PM patented in 1982 [13]. A few years later, adaptation of electric machine designs had begun. Among the rotor topologies suggested were: spoke type PM rotor, with tangentially magnetized magnets; surface mounted PM and buried PM rotors, both with radially magnetized PMs. One author described the NdFeB PM as "nearly ideal for the use in rotating machines" [3].

Development within both the field of permanent magnet synchronous generator (PMSG) design and PM material field is ongoing. Ferrite PM machines

have seen continuous research, due to low cost of the PMs; and rare earth metal PM machines, due to the promise of higher performance.

The abundance of the minerals needed for the NdFeB PMs that existed when they were first introduced [3] has, however, become less certain; causing an increase in cost of NdFeB PMs and supply insecurities. In response to this, as well as environmental concerns related to the raw materials extraction, there has been renewed research interest in using other PM materials, e.g. ferrite PMs as in Paper I; but also in the development of new PM materials, e.g. [14].

1.2 Related Projects at Uppsala University

The work for this thesis was conducted at the Division of Electricity at Uppsala University. The generator prototype in Paper I, II, V, and VIII is part of the wind power research at the division. The prototype was designed by Eriksson et al. [15] and built by Bülow who used it for e.g. experiments on stator iron losses [16]. There is also research on electrical machines for other applications in the Division of Electricity that are related to the work in the thesis. Part of the work has been part of an effort to decrease the dependence on RE elements for PMs in electrical machines, other parts of this effort include research on novel PM materials.

1.2.1 Wind Power Research at the Division of Electricity

The wind power research at the Division of Electricity is mainly focused on a direct drive vertical axis wind turbine (VAWT) concept. The main characteristics of the wind power concept is the use of passive stall control in a VAWT with a direct driven PMSG placed at the tower base. A review of the research done is given in [17] and an overview is given below.

The wind turbine rotor has three straight blades that are attached to the vertical axis by struts. The rotor is directly connected to the generator at the base of the tower via a long shaft. The vertical axis makes the turbine omnidirectional; this removes the need for a system to turn the turbine to face the wind. Placing the generator at the tower base instead of in a nacelle at the top of the tower relaxes constraints on mass and size of the generator. The passive stall regulation requires that the generator can apply a breaking torque at all points of operation; therefore the generator must be designed with a large overload capacity. Passive rectification of the generator output is used, which allows the speed of the generator to be easily controlled, as the voltage on the direct current (DC) bus is roughly proportional to the speed. The voltage on the DC bus can in turn be controlled by the inverter converting the power into alternating current that can be delivered to the power grid.

There are two open site research prototypes in the project. The first is a 12 kW turbine located at Marsta outside of Uppsala, Sweden. The second is a

200 kW turbine located at Torsholm near Falkenberg, Sweden. There is also a generator prototype for laboratory experiments, which originally was identical to the generator of the 12 kW turbine but has been retrofitted with a rotor of the design described in Paper I. The retrofit was made in order to test if generator rotor using ferrite PM could be designed to give similar performance as a rotor with NdFeB PM.

1.2.2 Electrical Machine Design at the Division of Electricity

In the Division of Electricity there are several projects relating to electrical machine design. The most closely related project is the studies on modeling PM demagnetization conducted by Sjökvist [18, 19, 20, 21]. In Paper VII, with Sjökvist as the main author, the ferrite PM rotor design presented in Paper I is compared to the original NdFeB PM rotor of the generator, designed by Eriksson et al. [15], with respect to demagnetization resistance.

There is also research on linear PM machines for wave energy applications. Lejerskog studied how the slot openings, or lack thereof, affects the cogging force in linear PM generators for wave power [22]. Ekergård did work on the use of ferrite PMs in linear generators and the required mechanical design [23]. Kamf and Hultman researched automation of the production of the linear generators [24, 25].

Further there is research on SGs for hydropower applications. Marcusson did work on prediction of the magnetic leakage fields in the end regions of SGs and the losses they cause [26]. Péres-Loya did work on the management of radial forces in SGs by segmentation of the field winding and control of the field current, as well as management of axial forces by use of magnetic thrust bearings [27].

1.2.3 Development of Novel Permanent Magnet Materials

The project resulting in this thesis started as part of a collaboration between departments within Uppsala University on mitigating the cost and supply insecurities of NdFeB PM. The substitution of NdFeB PM by ferrite PM discussed above is one approach. Another approach is the development of new PM materials that uses more abundant elements in their composition. The search for suitable compounds and processes for producing such materials has been conducted through an interdisciplinary collaboration of material theory, material chemistry, and solid state physics, see e.g. [14, 28, 29, 30]. The role of this thesis in the search for new materials has been to investigate how a newly developed material is best used in a PMSG and to some extent provide some guidance on what material properties to prioritize, which is done in Paper IV.

1.3 Overview of Electrical Machine Design Research

The design of PM electrical machines is a diverse field. Electromagnetism, structural mechanics, thermal management, material science and engineering, manufacturing and many other disciplines are needed. An early set of guidelines can be found in [8]. The application of the machine in question governs what properties are prioritized.

A wide range of modeling techniques are used in electrical machine design. The use of time-stepped finite element method (FEM) to calculate the magnetic field in a two dimensional (2D) approximation and coupled with external circuit equations, as in [31], is a common method. Some phenomena, such as the field in the stack ends, require three dimensional (3D) FEM to be modeled as they are neglected in the 2D approximation, see e.g. [32]. The problem solved using FEM can be formulated in different ways depending on what phenomena are of interest as described in [33] and there are also other numerical approaches to solving the electromagnetic field in the machine, such as using the finite reluctance approach described in [34]. Static FEM can be used to calculate parameters for analytical models as done in [35, 36, 37]. Purely analytical models are also still being developed and used as in [38], albeit with time-stepped FEM for verification. Models based on FEM for magnetic field calculations also need models of hysteresis in magnetic materials such as those described in [39, 40] to be able to capture the demagnetization of PMs properly. For modeling the thermal aspects of the machine and coolant flow, computational fluid dynamics are sometimes used [41].

All of the above described calculation methods assume more or less ideal geometry and material parameters. When manufacturing an electrical machine there will always be some deviations from the ideal, due to manufacturing tolerances. In [42] the possible consequences of manufacturing tolerances in a direct drive generator for wind power are discussed in general while [43] focuses on manufacturing tolerances of the PMs. In [44, 45, 46, 47] the impact of tolerances on the cogging torque of PM machines is examined.

Some research concerns the limits of what materials can handle. In [48] the limits on the achievable force density of low speed machines is investigated. There are also investigations into scaling laws of electrical machines for quick estimates of size and weight [49].

There are a lot of publications on various types of machine topologies. The radial flux machine with different types of rotors is the most common. The surface mounted PM rotor is one common design, mostly used with NdFeB PM or SmCo PM as it requires high remanence PMs to work well. The rotor consists of a magnetic ring with the radially magnetized PMs mounted the on surface, variations of this rotor structure occurs in e.g. [3, 50, 51, 52]. Another common design is the spoke-type PM rotor where the PMs are tangentially magnetized with soft magnetic poles between them to allow for magnetic flux concentration. This kind of rotor is sometimes also called tangential in-

terior permanent magnet (IPM) rotor and is mentioned in e.g. [1, 3, 53, 54]. One variation on the spoke-type rotor concept is to make the rotor longer than the stator to get flux concentration also in the axial direction as described in [55, 56]. The spoke-type rotor can also be used in PM machines with variable magnetization [57]. Other IPM rotor types have magnets that have the magnetization direction closer to the radial direction. These are sometimes named after the shape of the PM arrangement, such as I, V, W. The I-shape IPM rotor can be built by adding pole-shoes to a surface mounted rotor and all three rotor types are built with the PMs mounted in slots in a laminated rotor. Examples of this kind of rotor can be found in [3], where it is equipped with cage windings for line-start in motor applications, and in [1, 50, 51, 52, 53, 58, 59]. The IPM rotor structure, especially when there are multiple layers of PMs per pole, is sometimes similar to the PM assisted synchronous reluctance machine. The PMs can be arranged in a dovetail pattern to reduce mechanical stress in the bridges of the lamination [60]. There are also the claw-pole rotor and variants thereof where the magnets are axially magnetized and the magnetically soft iron "claws" direct the magnetic flux density into the air gap [1, 61]. Apart from the radial flux synchronous machine (SM) there are a few other types of SM such as the transversal flux and the axial flux machines [62, 63].

One application where PMSGs are common is in direct drive wind power as they allow for the overall system to be more efficient and reliable [62] than e.g. a doubly fed induction generator with power electronics and a gearbox as described in [64]. The kinds of PMSGs considered for direct drive applications are radial flux machines with surface mounted PM rotor or spoke-type rotor, axial flux machines, or transversal flux machines. Examples of surface mounted PM rotors are found in [62, 63, 65, 66, 67], and [68] which uses an outer rotor variant. Spoke-type PM rotors are described or used in [54, 62, 69]. In [63] structural material is taken into consideration when a transversal flux machine is compared to a surface mounted PM rotor radial machine. Axial flux machines are also discussed as a possibility for direct drive wind power in [62, 70].

1.4 Aim of the Thesis

The aim of this thesis is to investigate how to design rare earth free PMSGs, primarily for low-speed, high-torque applications such as wind power. Two approaches are used. The first is to study how to design a generator with ferrite PMs, which are cheap and abundant but have low performance compared to RE PMs. The ferrite PM approach is addressed in Paper I, II, and V. Paper VIII is also related to the use of ferrite PM but is not further discussed in the thesis summary. The second approach is to study how to best use new PM materials that may emerge and what kind of PM material properties that are useful for PMSG applications. This is done by parameterizing the PM material and then

optimizing three different PM rotor topologies for torque production. This is presented chiefly in Paper IV and some supporting methodology is presented in Paper III.

1.5 Outline of the Thesis

The thesis consists of a summary and seven papers. The summary covers the content of the first five papers, which covers the main body of the author's work underlying the thesis. Paper VII and VI have minor contributions from the author; most of the author's contribution to Paper VII is also covered in Paper I, and Paper VI is not much related to the rest of the work. Paper VIII has some overlap with Paper V and inclusion in the summary was deemed unnecessary.

The summary starts with an introduction concluded by this section, followed by chapters on theory and methods used. The results are then presented in the two following chapters. The first of these chapters presents the results relating to using ferrite PMs instead of NdFeB PMs in an experimental wind power generator. The second of the chapters presents the results from the investigation on how PM material properties and PMSG design interact. The chapters on the results are followed by chapters describing the conclusions drawn from the results, future work, a popular summary in Swedish, and acknowledgments. The list of references concludes the summary.

After the summary the papers follow. First comes the published papers covered in the thesis summary, ordered by publication date, followed by papers under review ordered by submission date. After these follows the papers not covered in the thesis summary, also ordered by publication date.

2. Theory

Throughout this thesis it is assumed that the electrical machine under consideration is placed with one end at the origin of a cylindrical coordinate system (ρ, φ, z) such that the axis of rotation coincides with the z-axis, unless otherwise specified. The machine has an active length l_{act}, thus the other end is at $\rho = 0, z = l_{\text{act}}$.

2.1 Electromagnetism and Rotating Electrical Machines

A generator is an electrical machine that converts mechanical work into electricity. A force is needed to perform work on something, in electromagnetism this force is given by the Lorentz force law

$$\boldsymbol{F} = q_e(\boldsymbol{E} + \boldsymbol{v} \times \boldsymbol{B}) \tag{2.1}$$

where q_e is the electrical charge of the particle the force acts on, $\boldsymbol{E}$ is the electric field, $\boldsymbol{v}$ is the velocity of the particle, and $\boldsymbol{B}$ the magnetic flux density.[1] The behavior of $\boldsymbol{E}$ and $\boldsymbol{B}$ is described by four differential equations known as Maxwell's equations:

$$\nabla \cdot \boldsymbol{B} = 0 \tag{2.2}$$

$$\nabla \cdot \boldsymbol{E} = \frac{\rho_{\text{e}}}{\varepsilon_0} \tag{2.3}$$

$$\nabla \times \boldsymbol{B} = \mu_0 \left(\boldsymbol{J} + \varepsilon_0 \frac{\partial \boldsymbol{E}}{\partial t} \right) \tag{2.4}$$

$$\nabla \times \boldsymbol{E} = -\frac{\partial \boldsymbol{B}}{\partial t} \tag{2.5}$$

where ρ_{e} is the volume density of electrical charge, ε_0 is the permittivity of free space, μ_0 is the permeability of free space, $\boldsymbol{J}$ is the current density, and t is time. In (2.1) it can be seen that the force caused by $\boldsymbol{B}$ will always be perpendicular to any displacement of a charged particle. Therefore $\boldsymbol{B}$ cannot directly perform work on a charge. Somehow using a concentration of charges to set up $\boldsymbol{E}$ as described by (2.3) is not practical when using mechanical work, as the resulting $\boldsymbol{E}$ is conservative. This leaves the non-conservative $\boldsymbol{E}$ induced

[1] $\boldsymbol{B}$ is sometimes also called the magnetic induction or magnetic field.

by a time-varying $\boldsymbol{B}$ according to (2.5) as the only feasible way to convert mechanical work into electricity.

The frequencies typically encountered in a generator are below 10^3 Hz. The magnitude of $\boldsymbol{E}$ is limited by insulation systems to about 10^8 V/m [71, p. 500]. The permittivity of free space is approximately 9×10^{-12} As/Vm. This gives the $\varepsilon_0 \frac{\partial \boldsymbol{E}}{\partial t}$ term of (2.4) an order of magnitude that is 10^1 A/m^2. At the same time the current density can be on the order of 10^7 A/m^2 in a copper conductor, and even higher on the boundary of a magnetic material. The $\varepsilon_0 \frac{\partial \boldsymbol{E}}{\partial t}$ term is therefore often neglected, which gives the quasi-magnetostatic approximation. The quasi-magnetostatic approximation is used in the reminder of this thesis.

2.1.1 The Generator Equation

The purpose of a generator is to convert mechanical power into electric power. To do this a voltage need to be induced. Faraday's law states that the circulation of the electric field, i.e. the electromotive force (EMF), around any closed path, ∂S, is equal to the rate of change of magnetic flux through any surface, S, bounded by that path:

$$\mathscr{E} = \oint_{\partial S} \boldsymbol{E} \cdot \mathrm{d}\boldsymbol{l} = -\frac{\mathrm{d}}{\mathrm{d}t} \iint_{S} \boldsymbol{B} \cdot \mathrm{d}\boldsymbol{S} \tag{2.6}$$

where $\mathscr{E}$ is the EMF, $\boldsymbol{E}$ the electric field, $\mathrm{d}\boldsymbol{l}$ a directed path segment of ∂S, t is time, $\boldsymbol{B}$ the magnetic flux density, and $\mathrm{d}\boldsymbol{S}$ a directed surface element with a unit vector oriented such that ∂S is traversed counter-clockwise when viewed from the positive side. This is (2.5) restated as an integral equation.

In a synchronous machine ∂S is taken to follow one phase of the stationary armature windings. Assume the generator to be placed in a cylindrical system of coordinates (ρ, φ, z) as described at the start of the chapter. To simplify the right-hand side surface integral of (2.6) three approximations are made: that $\boldsymbol{B} = \boldsymbol{0}$ outside of the machine ($z \notin [0, l_{\mathrm{act}}]$), that there is no axial variation of $\boldsymbol{B}$, and that each slot and the winding turns contained therein are small enough to be considered an axial line on the inner surface of the stator bore. Let $p = 2, 4, 6, \ldots$ be the number of magnetic poles of both the rotor field structure and the stator armature winding. If $\varphi = 0$ is placed at one side of a winding turn (2.6) can for one turn of the winding be written as

$$\mathscr{E}_{\mathrm{turn}} = -\frac{\mathrm{d}}{\mathrm{d}t} \int_{z=0}^{l_{\mathrm{act}}} \int_{\varphi=0}^{\tau_c} B_{\delta,\rho}(\varphi, t) \frac{D_{\mathrm{si}}}{2} \mathrm{d}\varphi \mathrm{d}z = -\frac{D_{\mathrm{si}} l_{\mathrm{act}}}{2} \frac{\mathrm{d}}{\mathrm{d}t} \int_{\varphi=0}^{\tau_c} B_{\delta,\rho}(\varphi, t) \mathrm{d}\varphi \tag{2.7}$$

where τ_c is the mechanical coil pitch angle, and $B_{\delta,\rho}$ is the radial component of $\boldsymbol{B}$ on the inner surface of the stator, which is a cylinder with the diameter D_{si}. It is reasonable to assume that $B_{\delta,\rho}$ is $4\pi/p$ periodic in φ for a given t and

that the time dependence is due to rotation with angular speed Ω. This allows $B_{\delta,\rho}(\varphi,t)$ to be written as

$$B_{\delta,\rho}(\varphi,t) = \sum_{h=1}^{\infty} \hat{B}^h_{\delta,\rho} \cos\left(h\frac{p}{2}\left[\varphi - \Omega t\right] - \check{B}^h_{\delta,\rho}\right) \tag{2.8}$$

where $\hat{B}^h_{\delta,\rho}$ is the amplitude of the hth harmonic component of $B_{\delta,\rho}$, and $\check{B}^h_{\delta,\rho}$ is the phase angle of the same harmonic component. Inserting the hth harmonic component from (2.8) into (2.7) gives

$$\mathscr{E}_{\text{turn},h} = -D_{\text{si}} l_{\text{act}} \hat{B}^h_{\delta,\rho} \Omega \sin\left(\frac{hp\tau_c}{4}\right) \sin\left(\frac{hp\tau_c}{4} - \frac{hp}{2}\Omega t - \check{B}^h_{\delta,\rho}\right) \tag{2.9}$$

as the EMF induced in a single turn.

A phase winding can be constructed connecting turns in series and parallel. In the ideal machine all parallel paths of a winding are identical. The voltage induced in a phase is therefore obtained by summing the voltage induced in all the turns connected in series, forming a branch of the winding, giving the RMS value of the induced phase EMF of harmonic order h as

$$\mathscr{E}^h_{\text{RMS}} = \frac{1}{\sqrt{2}} D_{\text{si}} l_{\text{act}} \hat{B}^h_{\delta,\rho} \Omega \sum_{\text{turns}} \sin\left(\frac{hp\tau_{c,\,\text{turn}}}{4}\right) \cos\left(\frac{hp\alpha_{\text{turn}}}{2}\right) \tag{2.10}$$

where α_{turn} is the difference in φ between the turn at hand and a reference turn for the winding, $\tau_{c,\,\text{turn}}$ is τ_c for the same turn, and the sum is taken for all in-series turns of a winding.

In literature the sum factor of (2.10) is usually separated into the total number of turns and a quantity called the winding factor. Let n_s denote the number of conductors per slot, q the number of slots per pole and phase, and c the number of parallel circuits. The number of turns in series per phase is then $n_s qp/(2c)$ and the winding factor is

$$k_{w,h} = 2c \frac{\sum_{\text{turn}} \sin\left(\frac{hp\tau_{c\,\text{turn}}}{4}\right) \cos\left(\frac{hp\alpha_{\text{turn}}}{2}\right)}{n_s qp} \tag{2.11}$$

for harmonic order h. This allows (2.10) to be written more compactly as

$$\mathscr{E}^h_{\text{RMS}} = \frac{1}{\sqrt{2}} D_{\text{si}} l_{\text{act}} \hat{B}^h_{\delta,\rho} k_{w,h} \frac{n_s qp}{2c} \Omega \tag{2.12}$$

or as

$$\mathscr{E}^h_{\text{RMS}} = \sqrt{2}\pi D_{\text{si}} l_{\text{act}} \hat{B}^h_{\delta,\rho} k_{w,h} \frac{n_s q}{c} f_{\text{el}} \tag{2.13}$$

where f_{el} is the electrical frequency. If τ_c is constant $k_{w,h}$ can be separated into the pitch factor $k_{p,h}$, which is equal to the sine term of the sum in (2.10), and the distribution factor $k_{d,h}$. The distribution factor compensates for the

phase difference between the EMFs of different turns when $q \neq 1$ and the turns belonging to the same winding are spatially distributed over multiple slots. The derivation of $k_{d,h}$ for the more common winding types can be found in most text on electrical machines, e.g. [71]. In (2.12) or (2.13) most of the fundamental aspects of, and dimensions of importance to, the EMF induction in a generator are summarized.

2.1.2 Magnetic Force and Torque

The force on objects exerted by $\boldsymbol{B}$ is of great importance in electric machine design. The torque between the stator and rotor is what facilitates the energy conversion. The magnetic forces can also be of great importance to the mechanical design, especially in low speed machines where inertial forces are smaller. In [71] two main principles of force calculations are presented: the principle of virtual work, and the Maxwell stress tensor $\boldsymbol{\sigma}$. The former is derived from the conservation of energy and gives the force or torque as the derivative of the magnetic energy with respect to the displacement, linear or angular as applicable. The Maxwell stress tensor will be presented in more detail below.

The full derivation of the Maxwell stress tensor can be found in more advanced textbooks on electromagnetism, e.g. [72] (where the derivation is done in centimeter-gram-second units). The starting point is (2.1) taken for a charge density distribution to get the force acting on the charge distribution per unit volume. By making substitutions using Maxwell's equations and vector analysis, one arrives at an expression for the electromagnetic force acting on the charged particles per unit volume and the change of momentum density in the fields that is the divergence of a second order tensor. This tensor is the Maxwell stress tensor. The elements are given by

$$\sigma_{ij} = \varepsilon_0 E_i E_j + \frac{1}{\mu_0} B_i B_j - \frac{\delta_{ij}}{2}\left(\varepsilon_0 E^2 + \frac{1}{\mu_0} B^2\right) \tag{2.14}$$

where i is the direction of component of the stress, j is the negative normal direction of the surface on which the stress is acting, δ_{ij} is the Kronecker delta function, and B and E are the component or magnitude of $\boldsymbol{B}$ and $\boldsymbol{E}$, respectively. A subscript indicating a direction means the component of the vector along that direction, and no subscript indicates the magnitude of the vector. The electromagnetic force acting on an arbitrary volume can then be calculated as

$$\boldsymbol{F} = \oiint_S \boldsymbol{\sigma} \mathrm{d}\boldsymbol{S} \tag{2.15}$$

where S is the closed surface bounding the volume on which the force is acting. Torque is calculated similarly but with the addition of a vector cross product between the lever arm and the integrand of (2.15).

2.2 Magnetic Materials

When dealing with magnetic materials on a macroscopic scale $\boldsymbol{B}$ is usually divided into two parts as

$$\boldsymbol{B} = \mu_0(\boldsymbol{H} + \boldsymbol{M}) \tag{2.16}$$

where $\boldsymbol{H}$ is the magnetizing field[2] and $\boldsymbol{M}$ is the magnetization of the material. These two components are separated by their origin, $\boldsymbol{H}$ is the field due to remote sources and $\boldsymbol{M}$ is the field due to magnetic dipoles in the field point. While both are usually given with the unit $\mathrm{A/m}$, giving $\boldsymbol{M}$ in $\mathrm{Am^2/m^3}$ could be more appropriate as it reflects that $\boldsymbol{M}$ is the density of magnetic dipoles per unit volume. For a more in-depth discussion of magnetic materials and physical mechanisms of magnetic materials the interested reader is referred to a textbook on the subject, e.g. [73].

Magnetic materials are classified after how $\boldsymbol{M}$ relates to $\boldsymbol{H}$. The three groups that can be distinguished by their macroscopic properties are: diamagnetic materials; paramagnetic materials, antiferrimagnetic materials, and antiferromagnetic materials; and ferrimagnetic materials and ferromagnetic materials.

If $\boldsymbol{M}$ is proportional to $\boldsymbol{H}$ and the constant is small the material is either paramagnetic if the constant is positive or diamagnetic if the constant is negative. The diamagnetism of materials used in electrical machines is usually so weak it is negligible, e.g. in copper $\boldsymbol{M}$ is on the order of $-10^{-5}\boldsymbol{H}$. The paramagnetism of materials in electrical machines can sometimes be strong enough that it needs to be included in the models but is still weak compared to feromagnetism and ferrimagnetism. Paramagnetic materials can be useful for structural parts that need to be located where it is not desired to have a magnetic flux. Antiferrimagnetic and antiferromagnetic materials have the same macroscopic behavior as paramagnetic materials but the underlying physics are different. For diamagnetic, paramagnetic, antiferrimagnetic and antiferromagnetic materials it is convenient to write the relationship between $\boldsymbol{B}$, and $\boldsymbol{H}$ as

$$\boldsymbol{B} = \mu_0\mu_\mathrm{r}\boldsymbol{H} \tag{2.17}$$

where μ_r is the relative permeability and $\boldsymbol{M} = (\mu_\mathrm{r} - 1)\boldsymbol{H}$. The quantity $\mu_\mathrm{r} - 1$ is called magnetic (volume) susceptibility.

Ferromagnetic and ferrimagnetic materials are used extensively in electrical machines, e.g. stator steel and ferrite PM, respectively. They are characterized by their ability to get strongly magnetized and they also exhibit hysteresis. When plotting $\boldsymbol{B}$ or $\boldsymbol{M}$ over $\boldsymbol{H}$, typically in a uniaxial case, the curve forms a loop. Such a loop is shown schematically in Figure 2.1. Depending on the character of the hysteresis the material is classified as either magnetically hard (wide loop) or magnetically soft (narrow loop). Magnetically hard materials tend to retain most of $\boldsymbol{M}$ even if $\boldsymbol{H}$ causing it is removed or reversed. These are used as PMs. Magnetically soft materials retain some small $\boldsymbol{M}$ when $\boldsymbol{H}$

[2] $\boldsymbol{H}$ is sometimes also called the magnetic field or the magnetic field intensity.

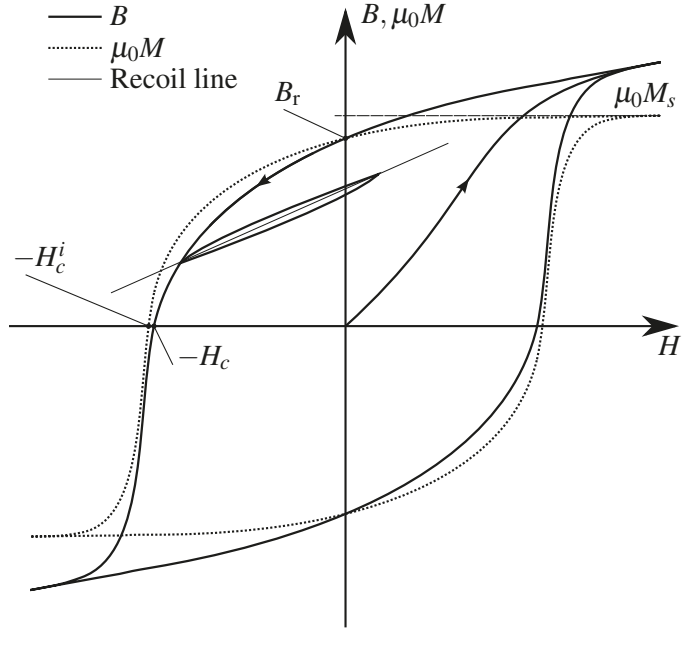

Figure 2.1. Schematic magnetization curve of a ferromagnetic or ferrimagnetic material in a one-dimensional case. B,M, and H are components of their respective corresponding vector along the same axis, B_r is the remanent magnetic flux density, M_s is the saturation magnetization, H_c is the (normal) coercivity, and H_c^i is the intrinsic coercivity. *Reused from the author's licentiate thesis [5].*

is removed and will easily align their $\boldsymbol{M}$ with any new $\boldsymbol{H}$. This makes them suitable for parts where a large $\boldsymbol{B}$ that changes is needed, such as in the stator core.

2.3 The Park Transform

The work in Paper III takes its starting point from the classical Two-reaction Theory of Synchronous Machines published by Park in 1929 [74]. The aspects of importance for the work at hand are the transformation of phase quantities to rotor quantities, the system of differential equations for the rotor quantities, and the assumptions that underlie the differential equations.

A typical electrical machine has three phases in the armature windings to allow balanced operation, give constant power, and eliminate the need for a neutral return conductor. Only two components are needed to describe the field in the air gap if neglecting the higher order spatial harmonics or as Park puts it "each armature winding may be regarded, in effect, sinusoidally distributed"[74], due to the orthogonality of sines. As the field structure on the rotor typically is the dominant source of magnetic flux density in an electrical machine it is useful to fix these two components to the rotor. The components are named the direct axis and the quadrature axis. The former is located in the middle of the magnetic pole of the rotor and the latter in between two poles.

Let the electrical rotor angle $\theta_{\text{rot}}^{\text{el}}$ be zero when the magnetic axis of the first phase aligns (denoted a) with the direct axis. The transformation from phase quantities is then given for the currents as

$$\begin{bmatrix} i_d \\ i_q \\ i_0 \end{bmatrix} = \frac{2}{3} \begin{bmatrix} \cos\left(\theta_{\text{rot}}^{\text{el}}\right) & \cos\left(\theta_{\text{rot}}^{\text{el}} - \frac{2\pi}{3}\right) & \cos\left(\theta_{\text{rot}}^{\text{el}} + \frac{2\pi}{3}\right) \\ \sin\left(\theta_{\text{rot}}^{\text{el}}\right) & \sin\left(\theta_{\text{rot}}^{\text{el}} - \frac{2\pi}{3}\right) & \sin\left(\theta_{\text{rot}}^{\text{el}} + \frac{2\pi}{3}\right) \\ \frac{1}{2} & \frac{1}{2} & \frac{1}{2} \end{bmatrix} \begin{bmatrix} i_a \\ i_b \\ i_c \end{bmatrix} \tag{2.18}$$

where i_d is the direct axis current, i_q the quadrature axis current, i_0 the zero axis current, and i_a, i_b, and i_c are the phase currents. The same transformation may be applied to phase EMFs, terminal voltages or the phase flux linkages. This transform is the Park transform or direct-quadrature-zero-axis (dq0) transform. The transformed quantities will here be referred to as the dq0 quantities.

If the eddy currents in the armature and saturation of the iron in the machine are neglected the terminal voltage and currents can be modelled by

$$\begin{aligned} v_d &= R_{\text{s}} i_d + L_d \frac{\mathrm{d}\, i_d}{\mathrm{d}\, t} - \omega_{\text{el}} L_q i_q \\ v_q &= R_{\text{s}} i_q + L_q \frac{\mathrm{d}\, i_q}{\mathrm{d}\, t} + \omega_{\text{el}} L_d i_d + \omega_{\text{el}} \psi_F \end{aligned} \tag{2.19}$$

where v_d is the direct axis terminal voltage, v_q is the quadrature axis terminal voltage, R_{s} is the resistance of one stator phase winding, L_d and L_q are the

synchronous inductance in the direct and quadrature axis, respectively, ω_{el} is the electrical angular frequency, and ψ_F is the magnetic flux linkage from the field structure.

2.4 The Finite Element Method

The finite element method (FEM) is a numerical method for solving partial differential equations (PDEs), boundary value problems such as Maxwell's equations or the equations of linear elasticity. The full derivation of the FEM is beyond the scope of this text but a short overview will be given here. The interested reader is referred to a textbook on the subject for the full theory, e.g. [75].

The general idea of FEM is to turn the PDE and the boundary condition (BC) into a system of linear equations. The first step to do this is to find what is called the weak form of the PDE by multiplying by another function and taking the integral of both sides. This other function is called the test function and should be bounded, as well as having a bounded gradient in the computational domain. Then the computational domain is subdivided into smaller regions of regular shape, typically triangles (in 2D cases) or tetrahedrons (in 3D cases). This subdivision is called a mesh. On the mesh, the set of piecewise polynomials form a basis in a finite dimension vector space of functions. A convenient set of basis functions takes unity value in one node, and zero in all other nodes. To proceed, one looks for the solution to the weak problem in the space of piecewise polynomials on the mesh and also takes the test function from the same space. A linear system of equations can be constructed for the nodal values of the solution by using the set basis functions suggested above. It can be shown that the error in the obtained solution is orthogonal to the space of piecewise polynomials, and from this it can be proved that it is the best approximation possible on the current mesh.

In the studies of this thesis the piecewise polynomials are usually of order one or two. Especially in 3D computations the first order is used as it requires less degrees of freedom per element.

Time-dependencies are usually handled by the method of lines. The method of lines uses FEM to discretize the PDEs in space and thus turn it into a system of ordinary differential equations (ODEs) or a differential-algebraic system of equations with initial values. Problems of these kinds are typically solved by finite-difference methods.

2.5 Potential Formulations of Maxwell's Equations

Maxwell's equations as stated in (2.2)–(2.6) form a coupled system of PDEs, which is cumbersome to solve. They are therefore reformulated in terms of

various potentials to make them easier to solve and remove unnecessary degrees of freedom.

There are two common potentials used when working with magnetic fields: the magnetic scalar potential ϕ_m and the magnetic vector potential $\boldsymbol{A}$. Which potential is the more useful depends on what situation is to be simulated. In 2D, the vector potential is usually always preferable as it is more versatile. In 3D, the scalar potential uses less degrees of freedom when using FEM to solve the PDE but it is less general, e.g. certain types of sources cannot be modeled.

2.5.1 Vector Potential Formulation

The magnetic vector potential $\boldsymbol{A}$ is defined by

$$\boldsymbol{B} := \boldsymbol{\nabla} \times \boldsymbol{A} \tag{2.20}$$

which ensures that $\boldsymbol{B}$ fulfills (2.2) as the divergence of the curl of a vector field is zero. In order to make $\boldsymbol{A}$ unique its divergence needs to be specified. A common choice is to use the Coulomb gauge and setting $\boldsymbol{\nabla} \cdot \boldsymbol{A} = 0$. A useful property of $\boldsymbol{A}$ is that it allows the non-conservative electric field to be calculated as

$$\boldsymbol{E} = -\frac{\partial \boldsymbol{A}}{\partial t} \tag{2.21}$$

where a conservative part of $\boldsymbol{E}$ can be added as a gradient of the scalar electric potential.

Radial flux rotating electrical machines have a geometry where the cross-section is constant in the axial direction for the entire active length of the machine. Also, most magnetically significant features in the cross section are small compared to the active length of the machine. Combined, the two above circumstances allows a 2D approximation of the machine to be used. For the 2D approximation, $\boldsymbol{B}$ is assumed to be entirely in the plane of rotation and $\boldsymbol{J}$ is assumed to be perpendicular to the same plane. From this, it follows that $\boldsymbol{A}$ only has an out of plane component A_z. As A_z does not change in z-direction, the Coulomb gauge condition is automatically fulfilled. The 2D approximation of the magnetic vector potential formulation is used in Paper I, II, IV, and V, as well is conceptually important to the work in Paper III .

To solve for $\boldsymbol{A}$ using FEM, it is convenient to linearize any constitutive relationship such that that

$$\boldsymbol{H} = \frac{\boldsymbol{B}}{\mu_\mathrm{r}\mu_0} + \boldsymbol{M} \tag{2.22}$$

where $\boldsymbol{M}$ is assumed only to depend on the location but not on $\boldsymbol{B}$ or $\boldsymbol{H}$. Insert (2.22) and (2.20) into (2.4) to get

$$\boldsymbol{\nabla} \times \left(\frac{\boldsymbol{\nabla} \times \boldsymbol{A}}{\mu_\mathrm{r}\mu_0} + \boldsymbol{M} \right) = \boldsymbol{J} \tag{2.23}$$

which under 2D approximation can be algebraically manipulated into

$$\frac{1}{\mu_\mathrm{r}}\nabla^2 A_z + \boldsymbol{\nabla}\left(\frac{1}{\mu_\mathrm{r}}\right)\cdot\boldsymbol{\nabla}A_z = -\mu_0\left(\boldsymbol{J}+\boldsymbol{\nabla}\times\boldsymbol{M}\right) \tag{2.24}$$

where $\boldsymbol{J}$ can contain both eddy currents and currents from external circuit couplings. The $\boldsymbol{M}$ term can be used to model the remanence of PMs, with μ_r set equal to the recoil permeability; or as the constant term of a Taylor expansion of the non-linear magnetization curve of a magnetically soft material where μ_r is then used for the first order term.

Ensuring that the Coulomb gauge condition is fulfilled in 3D typically requires an auxiliary scalar field to be solved for. Since there has not been a need for 3D simulations with conduction currents in the work underlying this thesis the magnetic scalar potential has been used instead.

2.5.2 Scalar Potential Formulation

The magnetic scalar potential can be used when $\boldsymbol{J}=\boldsymbol{0}$, as it is well known from vector calculus that if the curl of a vector field is zero everywhere, that vector field is the gradient of some scalar function. The magnetic scalar potential ϕ_m is defined by

$$\boldsymbol{H} := \boldsymbol{\nabla}\phi_m \tag{2.25}$$

and has the dimension of current. In free space and in regions with constant μ_r (2.25) and (2.2) combine to the Laplace equation for ϕ_m. Should there be a given $\boldsymbol{M}$ that is not proportional to $\boldsymbol{H}$, the equation turns into Poisson's equation with $-\boldsymbol{\nabla}\cdot\boldsymbol{M}$ as the source term. If μ_r is not constant in space, the differentiation operator gets problematic at first sight. However, when deriving the weak formulation for the FEM, the divergence operator is moved to the test function during the integration over the domain, by the use of Green's theorem, eliminating the problem. Ensuring uniqueness of ϕ_m is done by setting the value in at least one point in the domain or on the outer boundary.

3. Method

3.1 Finite Element Method Simulations of Electrical Machines

When using the finite element method (FEM) to simulate electrical machines for the work in this thesis the commercial implementation in COMSOL Multiphysics®[1] is used. The part of the implementation used is the "AC/DC-module" with the "Rotating Machinery, Magnetic" interface.

The geometries for the simulations are defined from geometric primitives, e.g. rectangles, circles, and polygons, together with geometrical set operations. The sizes of the geometric objects are set using parameters to allow for easy change of the geometry. Generation of the mesh for FEM is done by the built-in meshing tools of the software. Some restrictions on the element size are set to ensure that a sufficiently fine mesh is obtained in the air gap and other important parts while the rest of the geometry is meshed using the default options. Triangular and tetrahedral meshes are used in 2D and 3D simulations, respectively.

Common to all simulations of electrical machines performed is the use of periodic boundary conditions (BCs) on a minimal repeated sector to reduce the size of the computational domain. For the machine in Paper I, II, and V this means that only four of the poles, instead of all 32, need to be simulated. In Paper IV the number of poles that need to be simulated is two instead of 40. The radial boundaries with periodic BCs meet at the origin, removing the need for an inner constant radius boundary. On exterior boundaries where periodic BCs are not used the normal component of $\boldsymbol{B}$ is set to zero.

For all transient simulations the magnetic vector potential is used together with the 2D approximation, see (2.24), for reduced complexity and to ease mesh generation. The field solution obtained by FEM is coupled to an external circuit model where the FEM model is treated as a voltage source. The induced voltage is computed as the spatial mean of the electrical field in z-direction times l_{act} for each conductor and then summed with appropriate signs for all conductors of a phase. Stator winding resistance is treated as part of the external circuit model. The resulting current is applied as a constant current density in each conductor of the FEM model. In early implementations, i.e. Paper I, a direct coupling in the FEM model is used, which slowed down the computations. In the later implementations, i.e. Paper IV and Paper V, additional degrees of freedom for the currents are used, which decouples the

[1] See www.comsol.com

nodes of the FEM model, resulting in a sparser matrix and speeding up the computation. Eddy currents both in the windings and the magnetic steel of the stator and of the rotor are neglected by setting the electrical conductivity to zero everywhere.

For the stationary 3D simulations used in Paper V to investigate the magnetic end leakage fluxes, the magnetic scalar potential is used. To reduce the size of the computational domain the mirror symmetry around the $z = l_{\text{act}}/2$ plane is used. This is implemented by removing one half of the geometry and setting the normal component of $\boldsymbol{B}$ to zero on the mirror plane. Simulations with the 2D approximation using the magnetic scalar potential is also done for comparison to the 3D cases. First order elements are used to keep the number of degrees of freedom of the FEM model workable.

Forces and torques are calculated using the Maxwell stress tensor, see Section 2.1.2. For forces the built-in force calculation function of COMSOL Multiphysics® is used. This function simply integrates $\boldsymbol{\sigma}\mathrm{d}\boldsymbol{S}$ over the outer boundary of the domain for which the force is to be calculated. For torques Arkkio's method is used to improve accuracy [76]. This is a method for improving the accuracy when calculating the torque from fields computed using 2D FEM. Arkkio's method gives the electromagnetic torque as

$$T_{\text{em}} = \frac{l_{\text{act}}}{\mu_0 \delta} \iint_S \rho B_\rho B_\varphi \mathrm{d}\boldsymbol{S} \tag{3.1}$$

where the integration domain S is an annulus located in the air gap between stator and rotor, and of width equal to the air gap length δ.

3.2 Mechanical Modeling

The following section has previously appeared in the author's licentiate thesis [5].

In Paper I, the CAD (Computer Assisted Design) software SolidWorks® is used for geometrical and structural modeling of the designed generator. The geometrical modeling consists of creating 3D models of all the parts and then bringing them together in a model of the generator. This model is then used to make sure that all parts fit and do not overlap, and to make drawings for the workshop.

The structural modeling done is of two different kinds, both using simulation tools built into SolidWorks®. Volume meshes are used for both simulations, some less crucial parts are modeled as rigid or as a lumped mass, to speed up computation. The first type of simulation is static linear elasticity, which is used to check that neither excessive deformation nor material stress occurs. Input to the simulation is data on mechanical properties of the materials, allowed mechanical stresses and mechanical loads on the structure. The

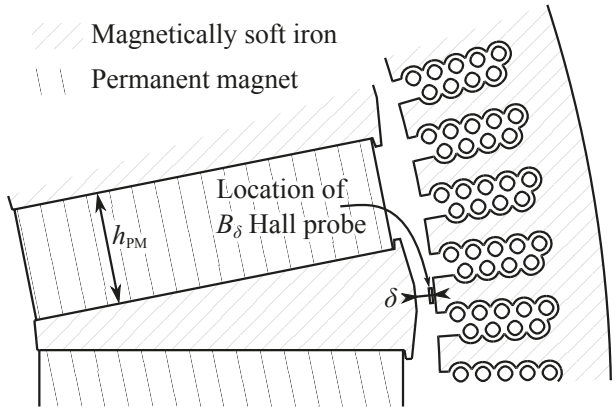

Figure 3.1. A 2D cross section of the magnetic circuit indicating some of the measured parameters; air gap length (δ), PM thickness (h_{PM}) and the location of the air gap magnetic flux density measurement (B_δ). Figure 1 from Paper II [77]. ©IEEE 2016.

second kind is a modal analysis to find the natural frequencies and associated modes of vibration. In addition to the data required for a static linear elasticity simulation this simulation needs the density of the materials. No dampening is included in the study which means that the frequencies will not be very accurate and that the magnitude of the vibrations cannot be predicted. The simulations will, however, allow the shape of the mode to be predicted; which, along with an approximate frequency, is enough for the current application.

3.3 Magnetic and Mechanical Air Gap Measurements

The following section has previously appeared in the author's licentiate thesis [5].

In Paper II measurements are performed on a generator to determine how manufacturing tolerances impact the magnetic flux density in the air gap. In Figure 3.1 the locations where the air gap length δ, permanent magnet thickness h_{PM}, and air gap magnetic flux density B_δ are measured are indicated. Measurement of B_δ is made with stationary rotor and only the radial component is measured. All of the above measurements are made for each of the 32 poles of the machine, using a fixed position on the stator and turning the rotor.

The magnetic flux density of a free-lying PM, $B_{\mathrm{free\ PM}}$, is measured in the middle of one pole surface of each PM. This was done prior to inserting the PMs into the rotor.

To measure the air gap length, a set of cylindrical tap gauges is used. The cylinder shape is chosen for two reasons. The first is that the stator laminations can be uneven and some averaging across multiple laminations is needed to get a representative air gap length, this makes a cylinder preferable to a ball

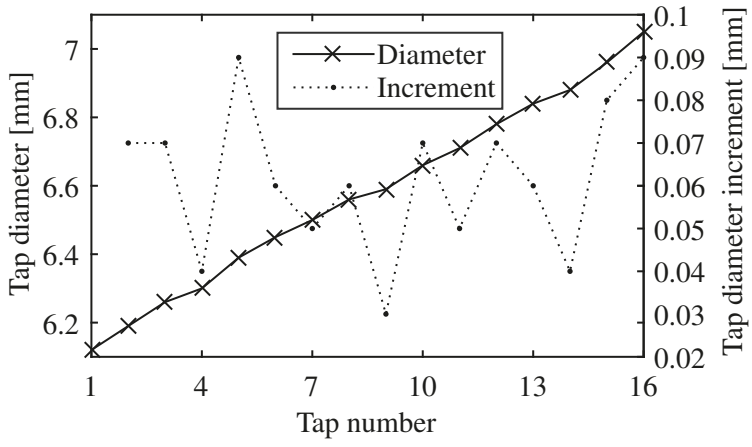

Figure 3.2. The diameters and diameter increments of the taps used to measure the air gap length. *Reused from the author's licentiate thesis [5].*

or disk. The second is that the air gap is curved, an ordinary flat feeler gauge would introduce a small systematic error due to the curvature of the stator bore.

The taps were made by turning in a lathe; new taps were made until a series with less than 0.1 mm between two taps was achieved. The diameters of the taps and the increments in diameter are shown in Figure 3.2. To perform the measurement of δ for a rotor pole the face of the pole and the stator tooth are wiped clean. Then taps of increasing diameter are inserted into the air gap until one that will not fit into the air gap is found. The diameter of the tap preceding this tap is then considered to be the air gap length. Some force applied by hand may be used to insert the tap.

The thickness of the PM, h_{PM}, was measured during the building process using a vernier caliper made of brass. The measurement is performed somewhere on the edge of the PM, usually in multiple places, and a single value or a range is recorded.

Both B_δ and $B_{\mathrm{free\,PM}}$ are measured using a FW Bell 5180 Gauss/Tesla meter. For the B_δ the probe is inserted about 50 mm from the upper end into the air gap in front of a stator tooth, as shown in Figure 3.1. The angular position of the rotor is then adjusted to maximize the reading to ensure the pole is exactly opposite the stator tooth. For $B_{\mathrm{free\,PM}}$ the center of the pole face is found by drawing two lines from opposing corners with a marker and then the measurement is made in the spot marked by the cross. This was done during the building process and the polarity of the PM was also checked in the procedure.

From $B_{\mathrm{free\,PM}}$, the B_{r} of each PM is calculated by a method described in Paper II. The mean value of the measured B_{r} and δ are inserted into the design simulations used in Paper I. The no load voltage is measured at 44 rpm and is also simulated, for comparison.

Error estimates for the measurements are made but omitted for brevity. The interested reader is referred to Paper II, section III for details.

3.4 End Region Magnetic Flux Density Measurements

The magnetic flux density in the end region is measured in Paper V. The measurement is performed with an FW Bell 5180 Gauss/Tesla Meter. The radial component of $\boldsymbol{B}$ along a line of constant ρ and φ, chosen such that the line passes in front of a stator tooth, is measured. The rotor is aligned to have the middle of the pole face the stator tooth. The axial position is changed in steps of 2 mm to span the distance from 52 mm inside the machine to 40 mm outside of the machine end, relative to the end face of the pole piece. A fixture made from a plastic ruler is used to keep the probe of the instrument on the line and measure the axial position. For further details on the measurements and instrument accuracy see Paper V, section IV-B.

3.5 Load and No Load Experiments on the Generator with Ferrite Permanent Magnet Rotor

In Paper V, the generator with the rotor design from Paper I and that is investigated in Paper II, is tested experimentally. The terminal voltage is measured both with and without any load connected. When a load is connected the currents are also measured. The three phase to neutral voltages are measured at no load, at several speeds up to the rated speed. Load cases include both full load and part load operation at rated speed. The load used is a purely resistive load. Two line to line voltages and two phase currents are measured and the power is calculated using the two-wattmeter method. For details on instrumentation used, measurement accuracy, and calibration of the measurements see Paper V.

In all measurements there are errors and these propagate to quantities calculated from measured values. Applying the formula for the propagation of the maximum error in a RMS value of a sampled signal x with N samples $x_i, (i = 1, 2, 3, \ldots N)$ calculated as

$$X_{\mathrm{RMS}} = \left(\frac{1}{N} \sum_{i=1}^{N} x_i^2 \right)^{1/2} \tag{3.2}$$

gives the maximum error in the RMS value as

$$X_{\mathrm{RMS}}^{\Delta} = \left(\sum_{i=1}^{N} |x_i x_i^{\Delta}| \right) \left(N \sum_{i=j}^{N} x_j^2 \right)^{-1/2} \tag{3.3}$$

where x_i^Δ is the error in the sampled value x_i. The error in the RMS value of the measured voltage and current is calculated using (3.3).

The same procedure can be applied to the mean power. When using the two-wattmeter method the power is given by

$$P(t) = v_{ab} i_a - v_{bc} i_c \tag{3.4}$$

where v_{ab} and v_{bc} are the line to line voltages between the phases indicated by the indices and i_a and i_c are the currents in the phases indicated by the indices. The error in mean power for N samples is then

$$P^\Delta = \frac{1}{N} \sum_{j=1}^{N} \left(|v_{ab,j}^\Delta i_{a,j}| + |v_{ab,j} i_{a,j}^\Delta| + |v_{bc,j}^\Delta i_{c,j}| + |v_{bc,j} i_{c,j}^\Delta| \right) \tag{3.5}$$

where v_{ab}^Δ, i_a^Δ, v_{bc}^Δ, and i_c^Δ are the maximum error in v_{ab}, i_a, v_{bc}, and i_c, respectively, and additional subscripts indicate that the quantity is sampled at the instant given by the subscript.

3.6 Winding Design Independent Short Circuit Current Calculation

Below is given an overview of the method for calculating the short circuit currents which is presented in Paper III, for full details see the paper. The method was developed as a tool to be used in the work resulting in Paper IV where there was a need for determining the short circuit currents without having to define a winding scheme.

3.6.1 Definition of Quantities

The treatment is done for a 2D approximation where calculations are made per unit length for a machine of indefinite length. In the cross section of some constant z there exists a surface S that represents the part of the cross section occupied by the winding. An auxiliary azimuthal coordinate

$$\varphi_{\text{el}} = \varphi p/2 + \theta_{\text{rot}}^{\text{el}} \tag{3.6}$$

is introduced.[2] The locations of S and $\varphi_{\text{el}} = 0$ in the cross section are indicated in Figure 3.3, note that $\varphi_{\text{el}} = 0$ follows the rotor when it rotates.

Assume that the out of plane current density J_z is sinusoidally distributed with respect to φ_{el} on S. This allows the direct and quadrature axis magnetomotive force (MMF) to be given by

$$\mathscr{F}_d = \hat{f}_{z,d} A_{\text{eff}} \tag{3.7}$$

[2]In Paper III θ_{el} is used for φ_{el}, this is changed in this text for consistency with the symbols used for the coordinates of the cylindrical system and to avoid confusion with $\theta_{\text{rot}}^{\text{el}}$.

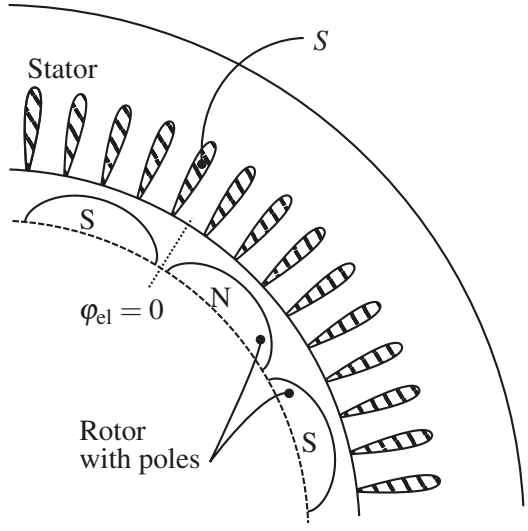

Figure 3.3. Conceptual sketch showing the location of $\varphi_{\mathrm{el}} = 0$ and the winding domain S (hatched areas). N and S indicate North and South poles of the rotor, respectively. Adapted from Fig. 1 from Paper III [78]. ©IEEE 2018.

and

$$\mathscr{F}_q = -\hat{J}_{z,q} A_{\mathrm{eff}} \,, \tag{3.8}$$

respectively, where $\hat{J}_{z,d}$ is the amplitude of the direct axis current density (cosine of φ_{el}), $\hat{J}_{z,q}$ is the amplitude of the quadrature axis current density (negative sine of φ_{el}), and A_{eff}, given by

$$A_{\mathrm{eff}} = \iint_S \cos^2 \varphi_{\mathrm{el}} \mathrm{d}S \tag{3.9}$$

is the effective winding cross section. From this follows that the magnetic flux that is linked to the direct and quadrature axis is

$$\Phi_d = \frac{1}{A_{\mathrm{eff}}} \iint_S A_z \cos \varphi_{\mathrm{el}} \mathrm{d}S \tag{3.10}$$

and

$$\Phi_q = \frac{-1}{A_{\mathrm{eff}}} \iint_S A_z \sin \varphi_{\mathrm{el}} \mathrm{d}S \,, \tag{3.11}$$

respectively.

The winding resistance per unit length, as seen from the magnetic circuit is

$$\varrho_{\mathrm{s}} = \frac{\rho_{\mathrm{el}}}{A_{\mathrm{eff}}} \tag{3.12}$$

where ρ_{el} is the resistivity of the winding corrected for the area fraction occupied by insulation instead of conductor.

3.6.2 The Short Circuit Model

The parameters defined in the previous section can be used in a system of ODEs of the same structure as (2.19). By setting the equivalent of the terminal voltages to zero, a symmetrical short circuit is obtained. This gives the following system of ODEs

$$\begin{aligned} 0 &= \varrho_{\text{s}} \mathscr{F}_d + \frac{\mathrm{d}\,\Phi_d}{\mathrm{d}t} - \omega_{\text{el}} \Phi_q \\ 0 &= \varrho_{\text{s}} \mathscr{F}_q + \frac{\mathrm{d}\,\Phi_q}{\mathrm{d}t} + \omega_{\text{el}} \Phi_d \end{aligned} \tag{3.13}$$

which can be linearized by setting

$$\Phi_d = \Lambda_d \mathscr{F}_d + \Phi_{\text{PM}} \tag{3.14}$$

where Λ_d is the direct axis permeance per unit length and Φ_{PM} is the magnetic flux due to the PMs linking to the direct axis, and

$$\Phi_q = \Lambda_q \mathscr{F}_q \tag{3.15}$$

where Λ_q is the quadrature axis permeance per unit length.

With the above linearization and the assumption of constant ω_{el} the system of ODEs in (3.13) has a closed form solution. In Paper III, it is computed by rewriting it on matrix form and using a matrix exponential to compute the solution, see Paper III for details.

The parameters for the linearization can be computed from two static FEM solutions of the magnetic field in the machine, one with no current in the windings to get Φ_{PM} and one with current in the windings to get Λ_d and Λ_q. The currents used in the second solution should be representative of the currents in the stator at a short circuit.

3.6.3 Validation

The method is validated against transient FEM simulations for three cases using two different machines in Paper III. The two machines are the 32-pole machine with the rotor from Paper I, and a preliminary design for a two-pole machine. The 32-pole machine was chosen because there were already simulations set up for it, and the two-pole machine was created to have different characteristics from the 32-pole machine, with regards to induced voltage and phase current. For details on both the machines, see Paper III, and Paper I for more details on the 32-pole machine. For the 32-pole machine a three phase

short circuit initiated from no load at rated speed is simulated. In the two-pole machine a three phase short circuit is simulated in two cases: one where the short circuit is initiated from no load, and one where it is initiated from rated resistive load.

The parameter estimation is done using three static FEM calculations of the magnetic field in the machine. The first is a no load case where there is no current in the windings. As $\mathscr{F}_d = 0$ in this case (3.14) gives $\Phi_{\mathrm{PM}} = \Phi_d$. The second is a load case where rated current is drawn by a resistive load. The Φ_{PM} obtained from the no load case is inserted into (3.14) and (3.15) together with Φ_d, Φ_q, $\mathscr{F}_d$, and $\mathscr{F}_q$ obtained from the load case. It is then trivial to solve (3.14) and (3.15) for Λ_d and Λ_q. The third FEM solution is a short circuit case where the currents used are calculated using Λ_d, Λ_q and Φ_{PM} obtained from the two first simulations. The final parameters for the short circuit calculations are then calculated using the result of the no load and short circut FEM calculation of the field. For the cases where the short circuit is initiated from rated load the initial values are taken from the rated resistive load FEM solution.

The results obtained with the method are compared to results obtained by transient FEM simulations of the respective cases. The comparison mainly focuses on the minimum value of $\mathscr{F}_d$ and maximum magnitude of $\mathscr{F}_q$, as well as the maximum total MMF as these are the most likely to cause demagnetization in PMs.

3.7 Rotor Topologies for Different Permanent Magnet Material Parameters

This section gives an overview of the method presented in Paper IV. The overall idea is to compare different PM material properties with respect to their usefulness in electrical machine design. This is done for three different PM rotor topologies. The PM materials are described by three parameters: the remanence B_{r}, the recoil permeability μ_{rec}, and the relative minimum magnetic flux along magnetization $C_{B_{\mathrm{PM}}^{\mathrm{min}}}$. The parameter $C_{B_{\mathrm{PM}}^{\mathrm{min}}}$ is used to describe the demagnetization resistance of the PM material, demagnetization resistance increases toward $-\infty$. The shape of the third quadrant magnetization curve given by the parameters of the PM material is shown in Figure 3.4.

The rotor topologies compared are surface mounted PM rotor, spoke-type PM rotor, and capped PM. The figure of merit for the comparison is torque per unit length and pole pair produced at resistive load and $45\,\mathrm{kA/m}$ electrical loading of the stator. The geometries of the rotor topologies and the stator are shown in Figure 3.5, for dimensions of the geometry see Table 2 of Paper IV.

Each of the three topologies is optimized with respect to PM size for a fixed amount of PM energy to find the highest torque under the specified conditions. The PM energy is computed as the product of the volume of PM material and the maximum energy product $|BH|_{\mathrm{max}}$ of the PM material, the

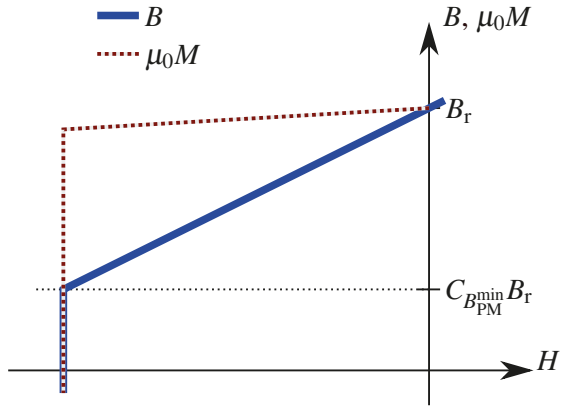

Figure 3.4. The third quadrant magnetization curve for a PM material parametrized by B_r, μ_rec and $C_{B_\mathrm{PM}^\mathrm{min}}$. The slope of the B curve is $\mu_\mathrm{rec}\mu_0$ and the slope of the $\mu_0 M$ curve is $\mu_\mathrm{rec}\mu_0 - 1$. Adapted from Fig. 1 of Paper IV.

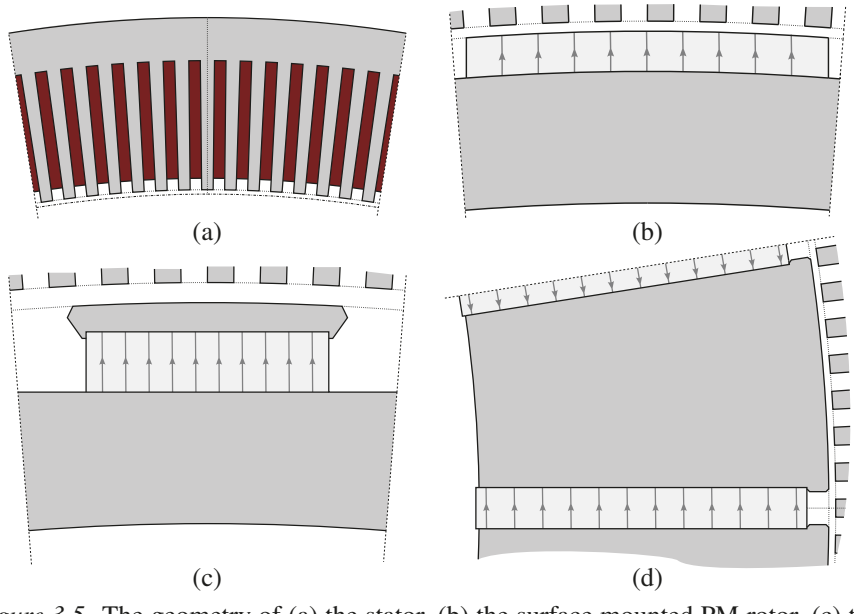

Figure 3.5. The geometry of (a) the stator, (b) the surface mounted PM rotor, (c) the capped PM rotor, and (d) the spoke type rotor used in Paper IV. The sub-figures are not of equal scale and the size of the PM only an example, the actual size is changed during the optimization. The dark gray areas are magnetically soft steel, light gray areas are the PMs with the arrow heads on the hatching indicating the direction of magnetization, and the dark red areas in (a) are the armature winding. Non-solid lines are indicate either the boundary between poles or various divisions of the simulation geometry that does not correspond to physical objects. Adapted from Fig. 2 through Fig. 5 of Paper IV.

value $164\,\mathrm{J/m}$ is used for one pole pair and unit length. The optimization is subject to the condition that the PMs are not demagnetized during a symmetrical short circuit. The stator current distribution during the short circuit is calculated using the method from Section 3.6 and Paper III, for more details on the demagnetization criteria see Paper IV. The values of the PM material parameters are $B_\mathrm{r} \in \{0.3, 0.4, \ldots, 1.5\}\mathrm{T}$, $\mu_\mathrm{rec} \in \{1, 2^{1/7}, 2^{2/7}, \ldots, 2\}$ and $C_{B_\mathrm{PM}^\mathrm{min}} \in \{-\infty, -0.2, 0, 0.2\}$.

There are many machine parameters that need to have their values set to make a machine design. Which values are used depend on the application, design principles, etc. In order to investigate how the choices of these machine parameters impact the generality of the results obtained, a sensitivity study is conducted. This is done by changing one of the machine parameters at the time from the default value. The same optimization as in the main study is then run on a sparser grid of material parameters. The parameters changed are pole pitch, air gap length, number of poles, linear current density in the armature winding, total PM energy, and the depth of the stator slots.

4. Design and Testing of a Rare Earth Free Permanent Magnet Rotor

The design for the rare earth free PM rotor in Paper I is presented below. This is followed by a summary of the results and discussion from the evaluation of the machine with the replacement rotor, presented in Paper II and Paper V.

The rotor design is to be used in an existing wind power generator prototype, described in [15], where it replaces a surface mounted PM rotor with NdFeB PMs. This means that the stator design is already fixed. The fixed stator design constrains the rotor diameter to a narrow span, and fixes the number of poles to 32 and the active length of the machine to 224 mm. Preferably the new ferrite PM rotor should also provide the same magnetic flux as the old NdFeB PM rotor. Finally, most of the frame design is to be reused, with minor adjustments.

Although mechanical and electromagnetic design are closely linked, it is convenient to separate them when presenting the result. Magnetic forces are, however, important to the mechanical design, and are therefore treated in the mechanical design section.

4.1 Electromagnetic Design Process

The following section has previously appeared in the author's licentiate thesis [5].

The first step in the design process of the replacement rotor is to choose rotor topology. Due to the low remanence of the ferrite PMs, flux concentration is needed. A spoke type rotor is therefore chosen.

An initial estimate of the size of magnet required is made to guide the search of suitable standard size PMs. The focus of the electromagnetic optimization made is to fit as much PM material as possible into the design.

The air gap face of the pole pieces has three flat sides that approximate a pole shape aimed to give a sinusoidal air gap $\boldsymbol{B}$-field distribution, described in [79]. This is intended as a compromise between ease of manufacture and achieving a good magnetic flux density distribution in the air gap.

4.2 Mechanical Design Process

The following section has previously appeared in the author's licentiate thesis [5].

Given the spoke type rotor topology a rough calculation of forces on the flux concentrating pole pieces are made. The forces are used to size the bolts that hold the pole piece in place. The six bolts with M4 thread made from A4-70 limit how narrow the pole piece can be at the inner end, the limit is used as a constraint in the electromagnetic design.

An isometric cut-away view of the final rotor design is shown in Figure 4.1. Solid poles are chosen for ease of assembly and structural reasons. Eddy currents are not expected to be a problem, due to large air gap length and low speed. The pole pieces, marked j in Figure 4.1, are bolted to the pole piece holders, b, and joined to the rotor bottom plate, c, using both bolts and slotted spring pins for alignment.

The pole piece holders are bolted to the rotor end plates, marked e and c in Figure 4.1 for top and bottom, respectively. The large stiffening rings, f, are fastened using the same bolts. The rotor end plates are held in place relative to the shaft, k, with flanges, a, that are bolted together to provide enough friction to transfer the torque. Alignment of the rotor plates is achieved using a tight fit between the shaft and the plate. Between the rotor end plates the inner supports, i in Figure 4.1, are placed. All parts are joined by bolts, to avoid welding. To avoid leakage fluxes support structure parts close to the pole pieces and PMs are made from aluminum. Another advantage of aluminum parts is that they are easy to handle, due to their low weight. The shaft, flanges and small stiffening rings are all far from the magnetic circuit and have structural requirements too high for aluminum to handle, and are therefore made of steel. Access to the interior of the rotor, in order to tighten bolts and for possible future experiments, is facilitated by holes in the rotor end plates.

The bearings are press-fitted onto the shaft and then mounted in steel housings. The steel housings are held by the generator end boards, made from fiberglass reinforced epoxy. Between the end boards and the stator there are metal bars fastened to the stator using dove tail keys and bolted to the end boards, not shown in Figure 4.1.

The pole pieces have the same length as the stator, 224 mm, while the PMs are slightly longer, 226.5 mm, due to wider tolerances. The PM blocks are 122.5 mm in the radial direction and 38 mm along the direction of magnetization. The PM material used is hard ferrite of grade Y40.

The extreme load, which the design should survive, occurs under a line to line short circuit. This is worse than both normal operation and three phase short circuit. During the line to line short circuit the maximum radial force on a pole piece is 2 kN and the torque on the rotor as a whole is 8.3 kN m. Another extreme load is the case of a misaligned rotor; the unbalanced magnetic

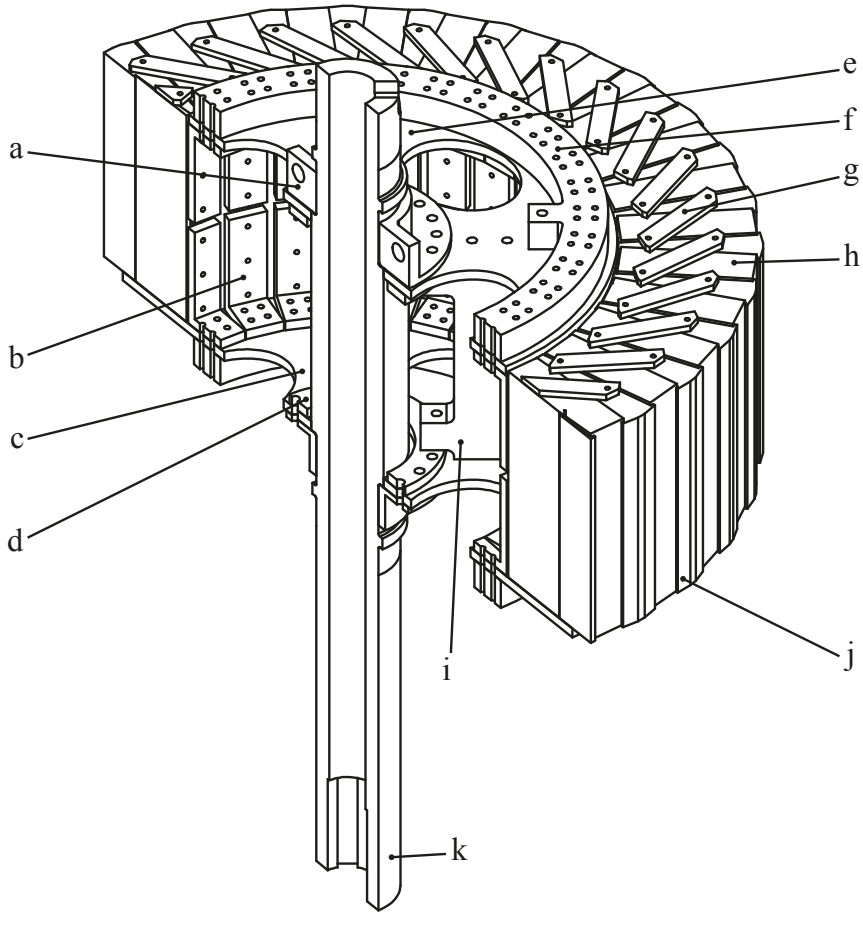

Figure 4.1. Isometric cut-away view of the ferrite PM rotor design. Half of the rotor has been removed to make the internal structure more visible. Parts indicated are: a) fastening flange, b) L-shaped pole piece holder, c) rotor bottom plate, d) small stiffening ring, e) top rotor end plate, f) large stiffening ring, g) bar for holding the magnet in place, h) permanent magnet, i) inner supports, j) pole piece, and k) shaft. All fasteners are omitted. Figure 1 from Paper I [80].

pull on a 3 mm off center rotor is 10 kN. This is a severe misalignment as the air gap length is 7 mm. The material thickness of the L-shaped pole piece holders, initially chosen as 10 mm due to availability, is calculated to be sufficient to withstand the loads with acceptable deformations. Also the shaft with a diameter initially chosen as 95 mm, same as for the old rotor, is calculated to be sufficiently strong to withstand the mechanical loads without excessive deformations.

The natural modes of vibration of the rotor installed in the generator are calculated with a slightly simplified geometry. The first mode is counteracted by the addition of the inner supports, see Figure 4.2.

The stiffening rings are also added to make the structure stiffer against higher order modes; for details, see Paper I. The outer diameter of the mid-part of the shaft is increased to make the shaft stiffer. The diameter of the central hole is also decreased for extra stiffness; ultimately a solid shaft was used, at the request of the workshop manufacturing the parts, to cut costs.

4.3 Predicted Electromagnetic Performance

The following section has previously appeared in the author's licentiate thesis [5].

The electromagnetic properties of the design are predicted by time-stepped FEM simulations. The simulated magnetic flux density in the generator at load is shown in Figure 4.3. The magnetic flux density in the air gap at no load is shown in Figure 4.4. The no load phase voltage is shown in Figure 4.5. A comparison of the new rotor design and the old rotor it will replace is given in Table 4.1.

The new rotor design is predicted to give a lower output voltage than the old design. In order to obtain the same power, a higher current can be drawn, since the electrical loading on the stator winding is low in the old design. This will increase the copper losses in the windings. At the same time the lower induced voltage is caused by a lower magnetic flux density in the stator, which will lower the iron losses. The total difference in efficiency of the generator will therefore be small at full load. The no load losses will, however, be lower for the new design, which should improve efficiency during part load compared to the old design.

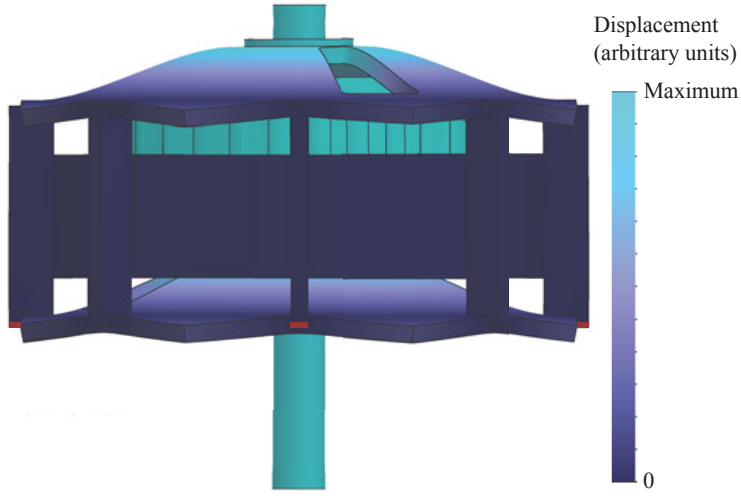

Figure 4.2. First natural mode of vibration. Deformations are not to scale and exaggerated to show the shape of the mode. The red boxes indicate where the displacement is set to zero. Figure 3 from Paper I [80].

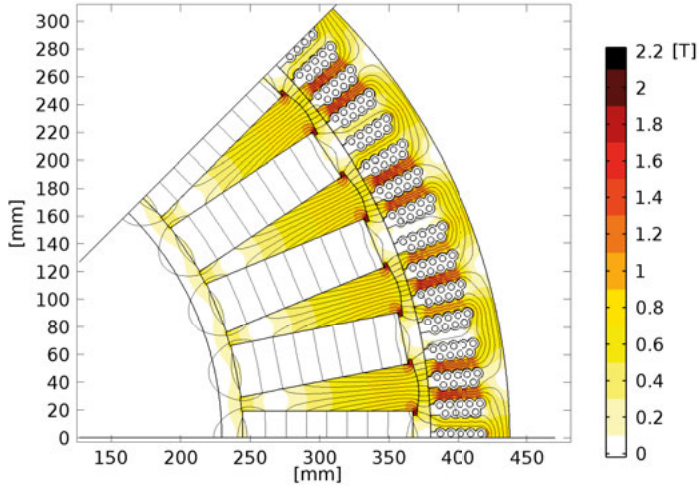

Figure 4.3. Magnetic flux density and field lines at load, for a 45° sector of the geometry, obtained through FEM simulations. The axes indicate position relative to the center of rotation and the color scale is magnetic flux density. Figure 4 from Paper I [80].

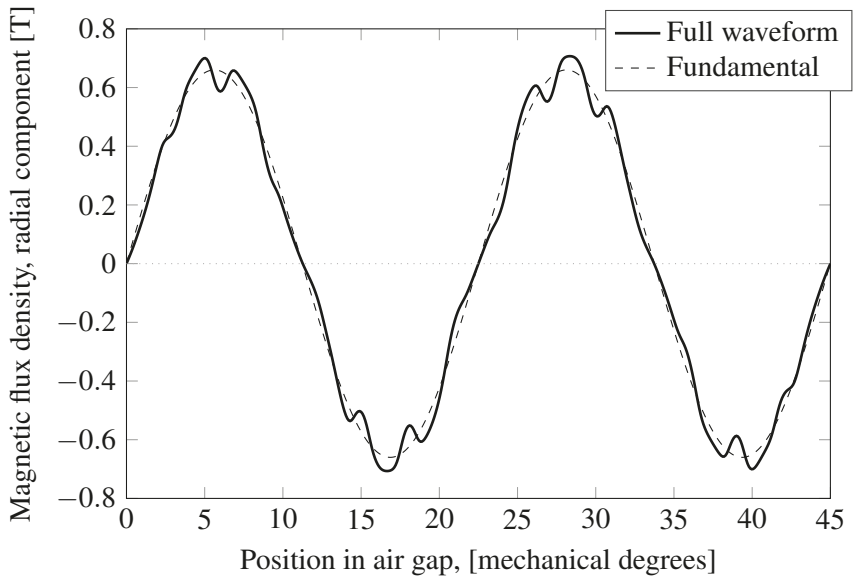

Figure 4.4. The radial component of the air gap flux density waveform and the fundamental of the waveform at no load, from FEM simulations. Adapted from Figure 5 in Paper I [80].

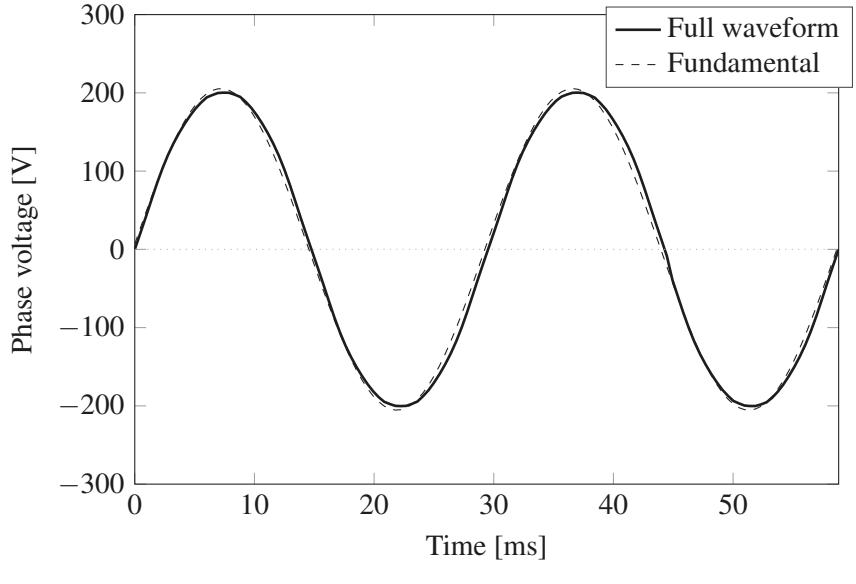

Figure 4.5. The phase voltage at no load with the fundamental shown, from FEM simulations. Adapted from Figure 6 in Paper I [80].

Table 4.1. *A comparison of the characteristics of the new design, using ferrite PMs, and the original design, using NdFeB PMs. Values are at rated load and speed. Data for the new design are from simulations. Data for the original design are from simulations except for weights. Data for the PMs are manufacturers' specifications (Sura Magnets AB, www.suramagnets.se, for the NdFeB PMs; and BJA Magnetics, http://www.bjamagnetics.com, for the ferrite PMs). Corrected version of Table 2 in Paper I [80]; the value of the maximum energy product for the PM material in the new design was incorrect in the data sheet of the manufacturer. Both designs are rated for a speed of 127 rpm and an electrical frequency of 33.9 Hz.*

Quantity	NdFeB (old) design	Ferrite (new) design
Rated power [kW]	12	12
Phase voltage, no load (RMS) [V]	172	146
Phase voltage (RMS) [V]	167	141
Armature current (RMS) [A]	23.9	28.5
Armature winding current density (RMS) [$\mathrm{A/mm^2}$]	1.49	1.78
Amplitude of air gap flux density fundamental at no load [T]	0.79	0.66
Resistive power losses [W]	275	390
Iron power losses [W]	254	159
Electromagnetic efficiency [%]	95.8	95.6
Minimum air gap [mm]	10	7
Mass of rotor [kg]	130	407
Mass of PM [kg]	41	158
Moment of inertia [$\mathrm{kg\,m^2}$]	16.9	34.2
PM material grade	N40	Y40
Remanence of PM [T]	1.27	0.45
Maximum energy product [$\mathrm{kJ/m^3}$]	310	37.6

4.4 Experiences from Building the Design — Discussion

The following section has previously appeared in the author's licentiate thesis [5].

One thing that was noticed when the rotor was built is the large number bolts and nuts that are hard to reach. While all of the fasteners could be properly tightened, using fewer and thicker bolts whenever possible would have been a better choice; in particular the bolts joining the pole piece holders, the large stiffening ring and the rotor end plates come to mind. There were also some problems with bolts getting stuck in threaded holes in some parts; if these problems should be avoided by designing joints to use nuts instead, use of

lubrication when fastening the bolts, or better quality control of the threaded holes should definitely be considered for future designs.

The bolts between the pole pieces and the holders should also have been thicker and fewer, but here there was a space constraint for the bolts. This would have required another design of the pole piece holders. These were designed under the erroneous assumption that the L-shape could easily be made, by cutting appropriate lengths of an extruded L-profile; this is not the case since extruded profiles do not have the required tolerances for the angle between the external faces. A possible alternative design is a design with one holder per pole, with a ridge extending in between the PMs. The ridge should reach so far that the inward face of the pole piece, mating with the top of the ridge, is wide enough to allow M5 bolts instead of the M4 bolts used. This will both make assembly easier by reducing the number of parts, and reduce the leakage flux in the interior of the rotor.

The solution for alignment of the pole pieces does not align the upper end of the pole pieces, which can have caused a shorter than nominal air gap length, see section 4.5.1. The easiest solution would probably be to add teeth extending out over the pole pieces to the upper rotor end plate, and join these to the pole piece with an alignment pin. Also, it might have been a better idea to use solid pins instead of the slotted spring-type pins used. This solution would, however, have made insertion of the PMs, which were thicker than tolerance, harder.

4.5 Experimental Results and Discussion

4.5.1 Manufacturing Tolerances and Air Gap Magnetic Flux Density

The following section has previously appeared in the author's licentiate thesis [5].

Selected properties of parts in the magnetic circuit of the PMSG have been measured, and are compared to nominal values. This is done to investigate how the properties impact the performance of the PMSG; as measured by magnetic flux density in the air gap and induced voltage. The cause of deviations from nominal values are discussed.

The per pole maximum air gap magnetic flux density, B_δ, is measured to between 572 mT and 639 mT. The mean of B_δ is 610 mT and it has a standard deviation of 16.7 mT. The magnetic flux density in the middle of the pole face of a free PM, $B_{\text{free PM}}$, is measured to between 61 mT and 79 mT, a suspected outlier measured to 36 mT was excluded. The mean of $B_{\text{free PM}}$, excluding the outlier, is 71.6 mT and the standard deviation is 4.6 mT. The air gap width, δ, is measured for a fixed point on the stator to between 6.26 mm and 6.96 mm. The mean value of the measured δ is 6.64 mm and the standard deviation is

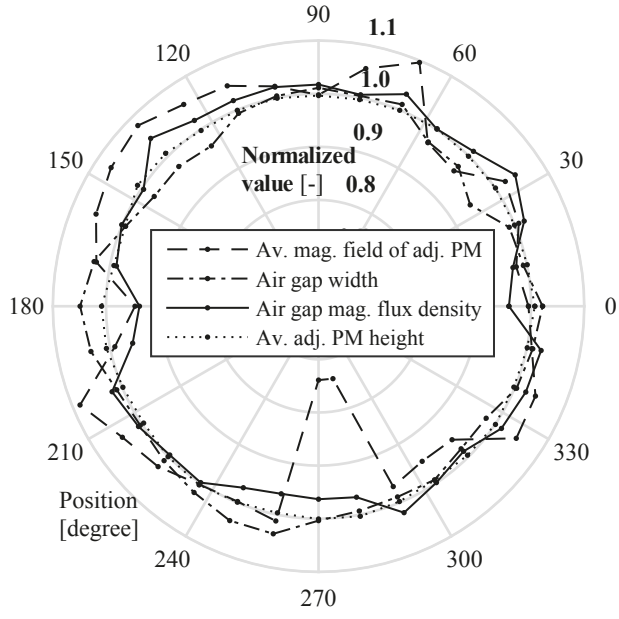

Figure 4.6. The measured parameters normalized by their respective arithmetic mean. Note that the radial scale have 0.6 at the center and not zero to make the variations clearer. Mean values used for normalization are 70.5 mT for $B_{\text{free PM}}$, 6.64 mm for δ, 610 mT for B_δ and 38.1 mm for h_{PM}. Figure 7 from Paper II [77]. ©IEEE 2016.

Table 4.2. *Correlation coefficients of measured parameters. Calculated with the outliers around* 276° *in Figure 4.6 removed. Table II of Paper II [77].* ©*IEEE 2016.*

	$B_{\delta,\rho}$	δ	$B_{\text{free PM}}$	h_{PM}
$B_{\delta,\rho}$	1	−0.65	0.51	−0.26
δ	−0.65	1	−0.15	0.057
$B_{\text{free PM}}$	0.51	−0.15	1	−0.023
h_{PM}	−0.26	0.057	−0.023	1

0.16 mm. The thickness of the PMs along the magnetization, h_{PM}, is measured to between 37.5 mm and 38.7 mm. The mean of h_{PM} is 38.13 mm and the standard deviation is 0.24 mm. The measurements on the generator are presented in normalized form in Figure 4.6, where the values given for properties of the PMs are the average of the PMs adjacent to the pole.

The correlation coefficients for the measured parameters are computed, and shown in Table 4.2. The data for the poles adjacent to the outliers around 276° in Figure 4.6 have been removed from the calculations. It can be seen that B_δ has the strongest correlation for each of the other parameters.

For δ and $B_{\text{free PM}}$ the correlation have the expected sign. $B_{\text{free PM}}$ is an indicator of B_{r} of the PM, a higher B_{r} should give a higher B_δ. A larger δ increases the reluctance of the magnetic circuit, which reduces B_δ. For h_{PM} the sign of the correlation is not expected, a thicker PM should provide a greater

Table 4.3. *Comparison of nominal and measured quantities. For nominal values, the ±-values are tolerances given by the manufacturer. The measured values are given as mean and maximum positive and negative deviation from the mean. The values in the "Verification" column shows the quantities used in (in italics), or calculated from, a simulation with δ and B_r from measurements. Table III from Paper II [80].* ©*IEEE 2016.*

Quantity	Nominal	Measured	Verification
Air gap width δ (mm)	7	6.6+0.3/-0.4	*6.6*
PM Thickness (mm)	38± 0.1	38.1+0.6/-0.6	*38*
B_r (T)	0.45±0.01	0.38+0.04/-0.06	*0.38*
$B_{\delta,\rho}$ (T)	0.70	0.61+0.03/-0.04	0.61
No load RMS phase voltage at 44 rpm (V)	50.4	40.9±0.1	44.0

excitation and give a larger B_δ. The cause of this is unclear but a qualified guess is that most of the variation in h_PM is caused by uneven thickness in the layer of adhesive, holding the sintered blocks of ferrite together to form the PM.

A comparison of the design simulation with nominal values, measurements, and a verification simulation, where measured values of δ and B_r are used, is shown in Table 4.3.

It can be seen that the parameter deviating the most from nominal is the remanence, which B_δ should be approximately proportional to. Multiplying B_δ from design simulations by the ratio of the estimated B_r and the one used in the design simulations gives a quite close estimate of the measured B_δ. It does, however, not fully account for the difference; which indicates that the air gap length and other parameters may also play a role.

When given the correct data the FEM calculations predict the magnetic flux density well. It does, however, fail to correctly predict the induced voltage; the difference is equivalent to what is induced in about 2.0δ to 2.5δ of machine length. This makes the need of correction for end effects in 2D simulations apparent.

It is remarkable how well the method of inferring the remanence from the field of a free PM, measured in a single point, works. By inserting the average remanence obtained by this method into the FEM simulation, along with the average air gap length, the prediction of the magnetic flux density in the measurement point in the air gap matches the measurement in the two first significant digits. While only a single test of the method has been made, the results obtained show promise.

4.5.2 Experimental Verification of Simulations and End Effects

Here is presented the findings from Paper V. A summarized comparison between the simulations, with the experimentally determined air gap length and

Table 4.4. *Comparison of measurements and simulations. Voltages and currents are given as the per phase RMS value of all phases. Voltages are line to neutral. Resistance is given as the mean of all phases. Adapted from Table II of Paper V.*

Quantity	Experimental	Simulated
Average power [kW]	12.0	12.1
No load voltage [V]	118	126.7
Full load voltage [V]	110	120.0
Full load current [A]	36.3	33.4
Phase resistance [mΩ]	149	150
Ohmic losses [W]	589	501
Synchronous inductance [mH]	3.1	3.03
Generator constant [V/rpm]	0.93	0.99

PM remanence, and the measurements is given in Table 4.4. The generator constant is the slope of the no load voltage over speed. In Paper V a more detailed version of Table 4.4 is given as Table II where the measured voltages, currents, and resistances are given per phase. An estimate of the maximum error is also given for all measured quantities, calculated according to the formulas given in Section 3.5 (see Table II of Paper V). The largest relative error is in the Ohmic losses with nearly 9 %, followed by average power (7 %) and the full load current (4 %).

The harmonic content of the no load voltage is low. In the experiments the strongest harmonic component, the third, has an amplitude of about a hundredth of the fundamental component. There are also components of orders $\frac{1}{2}, \frac{3}{2}, 6\frac{1}{2}$, and 7 that are not predicted by the simulations, all of these are on the order of a thousandth of the fundamental component, see Fig. of Paper V.

The measured waveforms of two line to line voltages, two phase currents, and the power at rated resistive load are shown together with their simulated counterparts in Fig. 7 of Paper V. The voltages and currents are mostly sinusoidal but some harmonics and some imbalance between phases can be discerned in the power which fluctuates over the period. The fluctuation is more irregular in the measurements than in the simulations. The regularity of the fluctuation in the simulated case makes it likely that it is mostly due to harmonics in the voltage. The frequency of six times the electrical frequency indicates that it is caused by torque ripple due to fifth and seventh order harmonics. The fluctuations in the experimental case exhibit these same fluctuations but also have components which seem to be due to imbalance between the phases.

It can be seen in Table 4.4 that there is a discrepancy between simulation and measurement of about 7 % in the induced no load voltage. As the air gap length and remanence of the PMs in the simulations have been set to the mean of the measured values obtained in Paper II, errors in these parameters should not be able to explain the difference. Also, the rotor is made to be of equal physical length as the stator which should rule out stacking effects as the cause of the discrepancies. Since the machine has a quite low ratio of ma-

chine length over stator diameter this hints that the end effects, not included in the 2D simulations, may be the cause. This is further supported by that in the spoke type rotor there are large end surfaces of the rotor pole pieces, which are more or less equipotentials for the magnetic scalar potential ϕ_m. The difference in ϕ_m between two adjacent poles is the largest there is in the magnetic circuit of the machine. The end surfaces of the pole pieces are therefore representing a rather large cross section for the magnetic leakage flux path. This represents a possible path for magnetic leakage flux that can have sufficiently low reluctance to be of importance, especially in short machines. The choice to simulate and measure the field in the end region is therefore justified.

The radial component of the magnetic field in the air gap and the end region of the generator is measured as described in Section 3.4. A 3D scalar potential solution for the magnetic field inside of the generator, and in the space surrounding it, is made using FEM, and the remanence of the PMs is tuned so that the magnitude of the radial component of $\boldsymbol{B}$ inside the stator matches the measurements. A 2D simulation is also made with a cross section of the geometry and the same material parameters. The measurements and simulation results are shown in Fig. 8 of Paper V. The measured value of the radial component of $\boldsymbol{B}$ is constant slightly less than 0.60 T inside the air gap of the generator, until it starts to smoothly transition to an exponential decay with axial distance outside of the machine. In the 3D simulation the remanence of the PMs is tuned so that the magnitude inside the stator is nearly equal to the 0.60 T in the measurements to facilitate easier comparison. The transition in the experimental data starts at about 10 mm inside the machine, measured from the end of the rotor pole pieces, and slightly later for the simulated data. The 2D simulation gives the radial component of $\boldsymbol{B}$ as about 0.65 mT for the same remanence as the tuned 3D simulation. The ratio of the radial component of $\boldsymbol{B}$ from the 3D and 2D simulations is quite close to the ratio of the no load voltage from experiments and simulations. This further indicates that the magnetic end leakage flux is the cause of the lower than expected voltage.

When changing the length of the machine in the simulations, the magnitude of the radial component of $\boldsymbol{B}$, inside the stator, in the 3D case follows that of a rational function with first order polynomials of the machine length as both nominator and denominator. Fitting a function of this form to 3D simulation data and extrapolating to infinite machine length predicts the 2D result closely. The structure of the function can also be motivated using a simple equivalent circuit model.

5. Electrical Machine Design for Parametrized Permanent Magnet Materials — Results and Discussion

In this chapter the findings from Paper III and Paper IV will be presented and discussed. The short circuit current calculation method presented in Paper III was developed as a part of the work underlying Paper IV.

5.1 Validation of Winding Design Independent Short Circuit Current Calculation

Comparisons of the MMFs during a short circuit event obtained via the model proposed in Paper III and Section 3.6, and the MMFs obtained using transient FEM are shown in Figure 5.1. The largest difference between the model and transient FEM in minimum value of $\mathscr{F}_d$ is 12.5 %, which happens for the 32-pole machine. The largest difference in maximum magnitude of $\mathscr{F}_q$ is 25 %, which happens for the two-pole machine when the short circuit is initiated from no load.

Considering the idealization behind the model, compared to the transient FEM simulations, the above differences are reasonable. Also, the error made is conservative, since the model is developed to provide estimates of the short circuit current for use in demagnetization studies and all of of the errors are overestimates. As seen in Figure 5.1 there is also some difference in the timing of the maximum quadrature axis current magnitude and minimum of the direct axis current, but as the model is mainly intended to find the value of the extreme current this is not a major concern.

The two machine designs used are quite different. The two-pole machine has low voltage and high current and the other machine has high voltage and low current. This indicates that the validation results should hold for a wide range of PM synchronous machines.

5.2 Permanent Magnet Rotor Topology Comparison

Here a subset of the results of Paper IV will be presented. For the full result see Paper IV.

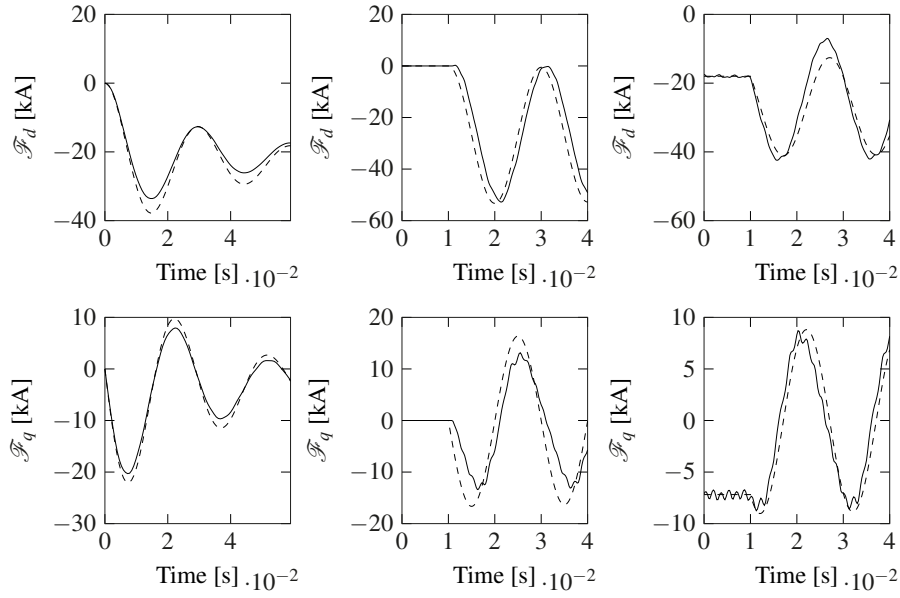

Figure 5.1. Comparison of $\mathscr{F}_d$ and $\mathscr{F}_q$ during a short circuit computed using transient FEM simulation with circuit model (solid line) and using the model presented in Section 3.6 and Paper III (dashed line). The different cases are short circuit events in: (a) the 32-pole machine starting from no initial current, (b) the two-pole machine starting from no initial current, and (c) the two-pole machine starting from resistive load and rated current. Adapted from Fig. 5 through Fig. 7 of Paper III [78].

The torque per pole pair and unit length in the most demagnetization sensitive materials, given by $C_{B_{\mathrm{PM}}^{\min}} = 0.2$, as a function of B_{r} and μ_{rec} is shown in Figure 5.2 as a set of level curves. In Paper IV a more detailed version of Figure 5.2 is found in Fig. 7, as well as the corresponding plot for $C_{B_{\mathrm{PM}}^{\min}} = -0.2$ in Fig. 8. In Figure 5.2 some parts of the PM material parameter space are missing. There are three causes for this: the given amount of PM material does not fit into the rotor topology, the combination of PM material and rotor topology cannot be configured to meet the required load condition, or the rotor cannot be configured to resist demagnetization for the amount of PM material and PM material parameters.

The spoke type rotor shows high torque in the regions where the demagnetization can be handled. The missing parts in the lower part of the spoke type torque plot are mostly due to failure to resist demagnetization, except for a few points on the $B_{\mathrm{r}} = 0.3\,\mathrm{T}$ line which are due to lack of space for the PM. When increasing the demagnetization resistance, by setting $C_{B_{\mathrm{PM}}^{\min}} = -0.2$, the region where the demagnetization can be avoided increases considerably (Fig. 8 of Paper IV). The torque increases for lower values of B_{r} such that the region

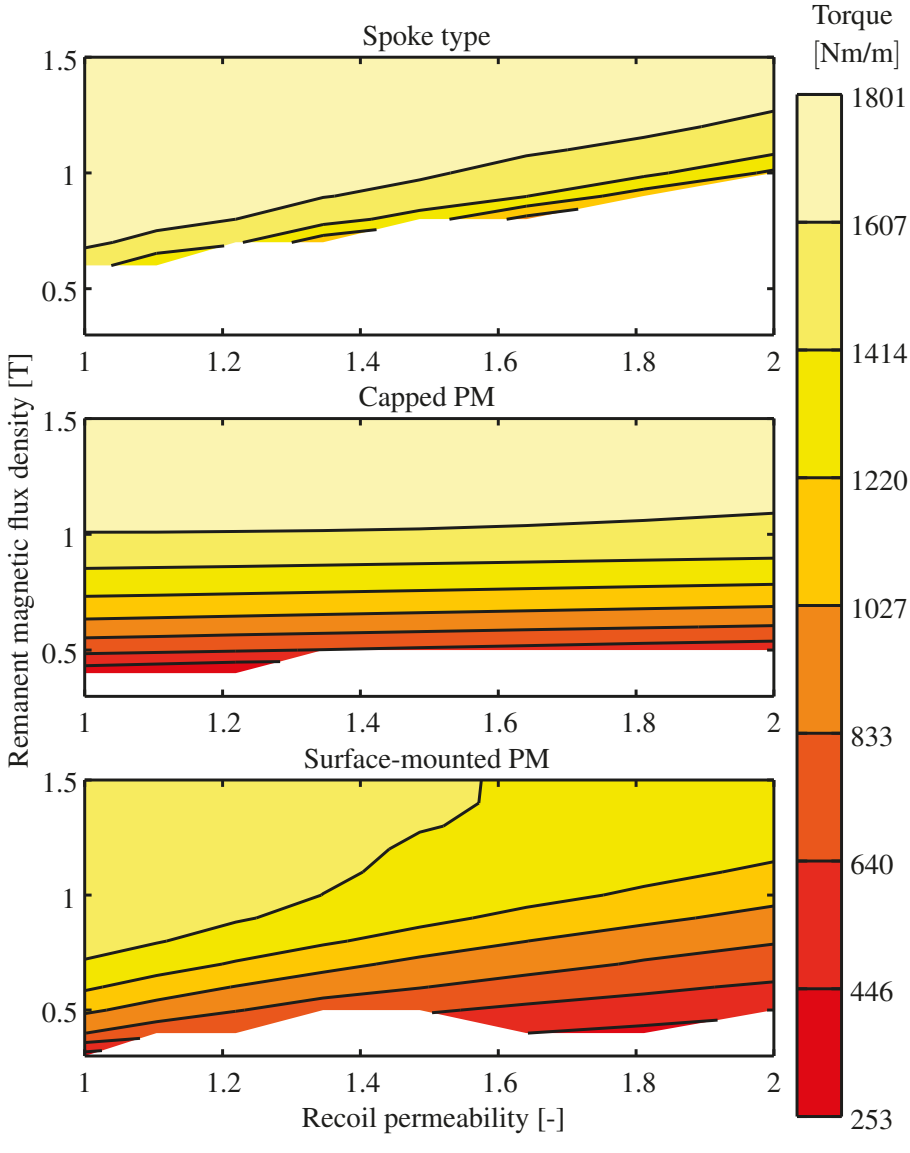

Figure 5.2. Torque per pole pair and unit length as a function of remanent magnetic flux density and recoil permeability for demagnetization parameter $C_{B_{\mathrm{PM}}^{\mathrm{min}}} = 0.2$. Color scale is shared between the subplots. Adapted from Fig. 7 of Paper IV.

with the highest torque shifts from the upper left part to a band around a line from approximately $(B_\mathrm{r}, \mu_\mathrm{rec}) = (0.5\,\mathrm{T}, 1)$ to $(B_\mathrm{r}, \mu_\mathrm{rec}) = (1\,\mathrm{T}, 2)$.

The capped PM rotor has high torque for high B_r, but the torque decreases for lower values of B_r. The missing parts of the plot for low B_r are mostly due to failure to reach the operating point. Very little in the distribution of the torque changes as the demagnetization resistance is increased except that the dependence on μ_rec decreases slightly (Fig. 8 of Paper IV).

The surface mounted PM rotor also gives its highest torque for high B_r materials with low μ_rec. As with the capped PM rotor, the μ_rec dependence decreases as the demagnetization resistance is increased (Fig. 8 of Paper IV). Unlike the capped PM rotor, the torque of the surface mounted PM rotor increases considerably for higher values of B_r when the demagnetization resistance is increased. This indicates that the surface mounted PM rotor offers very little protection against demagnetization. The lower protection against demagnetization means that the PM is constrained to suboptimal shape by the requirement to avoid demagnetization in the more demagnetization sensitive cases, resulting in lower torque.

In Figure 5.3 the torque per pole pair and unit length of the different rotor topologies is plotted over B_r, $\mu_\mathrm{rec} = 1$, for the case where demagnetization is not considered and for intermediate demagnetization resistance given by $C_{B_\mathrm{PM}^\mathrm{min}} = 0$. Figure 5.3 highlights how the different topologies perform when the demagnetization resistance of the PM is changed. The capped PM rotor shows no change at all. The surface mounted PM has a large decrease in torque for the B_r for which it had the highest torque when not considering demagnetization. The spoke type rotor gives higher torque on the lower end of the B_r axis, with only a slight decrease before demagnetization becomes unmanageable in the $C_{B_\mathrm{PM}^\mathrm{min}} = 0$ case. If demagnetization can be managed the spoke type rotor is well suited for low B_r materials, such as ferrite PMs, thanks to the flux concentration. Also, the increased volume of PM material allotted increases the separation between the pole pieces and thereby decreases magnetic leakage flux which results in a higher torque; the increased volume of PM material is allotted to keep the product of PM volume and maximum energy product $|BH|_\mathrm{max}$ constant.

Figure 5.4 shows which topology that gives the highest torque in each material point for the most demagnetization sensitive case, $C_{B_\mathrm{PM}^\mathrm{min}} = 0.2$. The volume of PM material is also indicated in the figure. Missing material points are due to the same reasons as for Figure 5.2. For the high B_r materials the capped PM rotor gives the highest torque. The spoke type rotor has a triangular region where it gives higher torque than the other topologies. To the low B_r side this region is bounded by the inability of the spoke type rotor to accommodate a PM that can resist demagnetization and on the high B_r side it is bounded by the capped PM giving higher torque. The surface mounted PM rotor gives the higher torque than the other topologies for materials with low B_r. This is

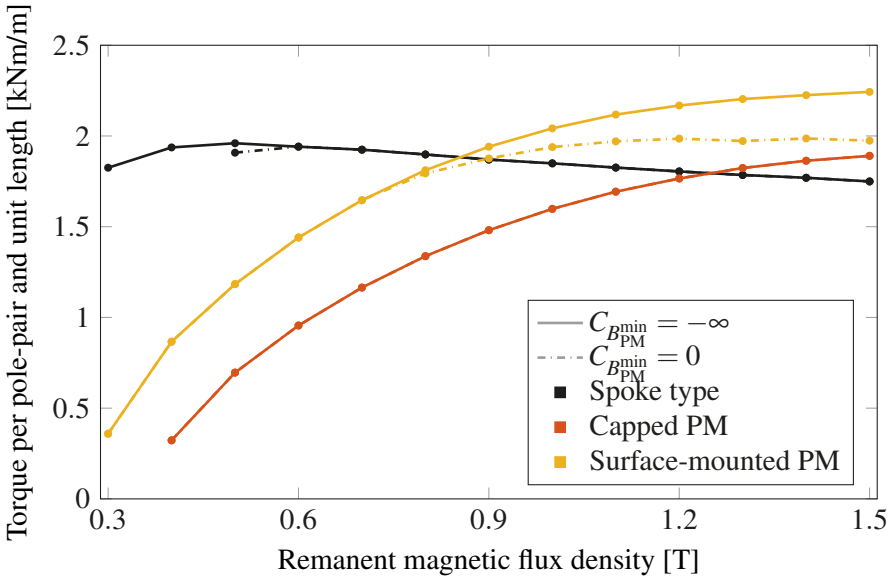

Figure 5.3. Torque per pole pair and unit length over remanence B_{r} for recoil permeability $\mu_{\mathrm{rec}} = 1$ and two demagnetization sensitivities given by $C_{B_{\mathrm{PM}}^{\mathrm{min}}}$. Adapted from Fig. 9 of Paper IV.

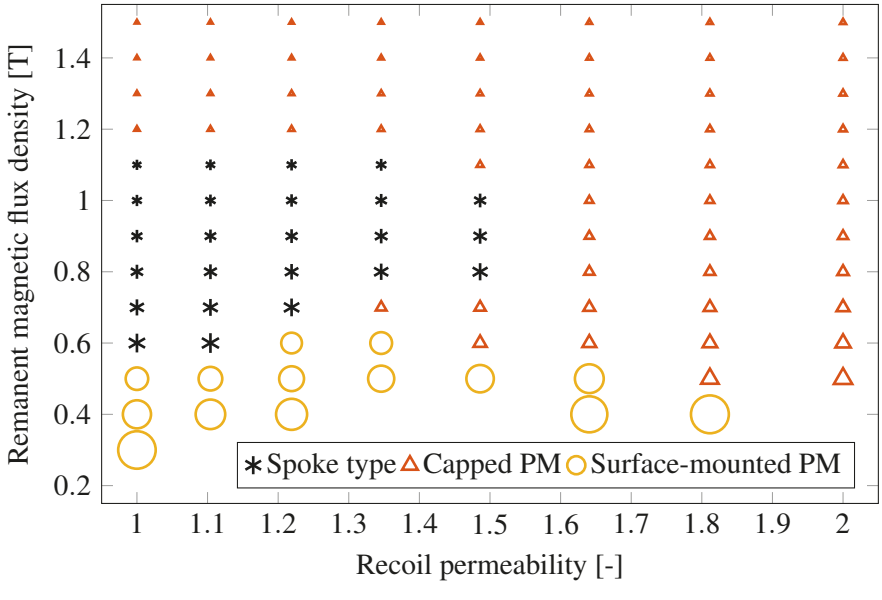

Figure 5.4. The topology that gives the highest torque per pole pair and unit length for each pair of μ_{rec} and B_{r} used, for demagnetization sensitivity given by $C_{B_{\mathrm{PM}}^{\mathrm{min}}} = 0.2$. Size of marker indicate amount of PM material used. Adapted from Fig. 10 of Paper IV.

mainly due to that the spoke type rotor cannot be made to withstand demagnetization for these materials due to geometric constraints on the length of the PM (along magnetization). The other rotor topologies do not geometrically constrain the length of the PM in the same way, allowing demagnetization to be resisted but at the cost of quite low torque. When the demagnetization resistance is increased by setting $C_{B_{\mathrm{PM}}^{\mathrm{min}}} = -0.2$, as shown in Fig. 11 of Paper IV, the capped PM rotor no longer gives the highest torque for any combination of μ_{rec} and B_{r}. For $C_{B_{\mathrm{PM}}^{\mathrm{min}}} = -0.2$ the spoke type rotor gives the highest torque of the three topologies for about $B_{\mathrm{r}} \leq 0.8\,\mathrm{T}$ and for higher B_{r} the surface mounted PM rotor gives the highest torque (Fig. 11 of Paper IV).

The results presented above and in Paper IV show that the spoke type rotor is the best option, with regard to torque production, for low B_{r} PMs, and that the surface mounted PM rotor is the best option for high B_{r} materials, as long as demagnetization can be managed. If the material has higher sensitivity to demagnetization, the capped PM rotor is a better option. The demagnetization sensitivity of the spoke type rotor when used for low B_{r} can partially be due to self-demagnetization of the PMs as they are constrained to be rather short (along the magnetization) by the rest of the geometry. With more degrees of freedom in the optimization this could probably increase the region where the spoke type rotor is usable. Also a more refined modeling of the demagnetization, such as in Paper VII, could show that a spoke type rotor with small partial demagnetization of the PMs still performs better than the other topologies. Additional degrees of freedom could also improve the performance of the capped PM rotor and spoke type rotor, as the shape of the pole shoe or the pole piece has been kept fixed during all the optimizations.

The sensitivity analysis is presented in Fig. 13 of Paper IV and indicates that the results have the most sensitivity to the choice of pole pitch and air gap length. For the pole pitch the practical sensitivity is lessened as changing the volume of PM material to maintain geometric similarity will approximately cancel the impact of changing the pole pitch. The torque produced by the spoke type rotor is more sensitive to changes in air gap length than the torque produced by the other two topologies.

6. Conclusions

In this thesis, the design of rare earth (RE) free permanent magnet synchronous generators (PMSGs) is approached from two different angles. The first is the use of the existing ferrite permanent magnet (PM) material and adapting a machine design to achieve performance similar to what can be achieved with neodymium-iron-boron (NdFeB) PMs. The second is to investigate how to design PMSGs for novel PM materials by studying how different PM material properties work with different rotor topologies.

A ferrite PM rotor can replace a surface mounted NdFeB PM rotor in a small, experimental wind power generator if a flux concentrating spoke type rotor is used. A slightly lower voltage will be induced which requires a higher current for the same power. The spoke type rotor is more mechanically complex than the rotor it is replacing and also heavier. While the increased weight of the generator is a drawback, it comes with an increased moment of inertia which is beneficial for the control of the generator and turbine system.

The ferrite PM rotor design is built and tested. The measured magnetic flux density in the air gap is found to be lower than the design simulations indicate it should be. From measurements the PMs are found to have remanence below specification, which explains a large part of the discrepancies between the design simulations and measurements. This highlights the importance of ensuring that material properties are within specification. It can also be concluded that measuring the magnetic flux density on the surface of a free-lying PM is a useful method for estimating the remanence of the PM if it can be assumed to be homogeneously magnetized.

Measurements of the no load voltage reveal that some discrepancy between the two dimensional (2D) simulations, and the experiments remains, even after inserting the measured values for PM remanence and air gap length. This discrepancy can be satisfactorily explained by the end leakage flux, which is not modeled in the 2D finite element method (FEM) models used in the design simulations. To capture this behavior either three dimensional (3D) FEM simulations or some analytical model is needed. The dependence of the machine length on the impact of the magnetic end leakage flux on the magnetic flux in the air gap can be modeled using a simple equivalent magnetic circuit model. The simple magnetic circuit model predicts the results of the 2D simulations well when fitted to data from the 3D simulations used to investigate the end leakage flux, and extrapolated to infinite machine length. This is concluded to be a possible approach to develop a method to improve the accuracy of the 2D approximation when modeling spoke type rotors.

The winding design independent method for calculating the short circuit currents in a PM synchronous machine (SM) is found to be useful for its particular purpose. Its purpose is to give a rough estimate of the armature magnetomotive force (MMF) for demagnetization estimates done early in the design process of a PM SM when the winding design has not yet been finalized.

From the study on what rotor topology to use in a PMSG for a PM material defined by the remanence, recoil permeability, and demagnetization resistance a few conclusions can be drawn. The three rotor topologies are useful for different types of PM materials. The spoke type rotor is the rotor topology that gives the highest torque with low remanence materials. It does, however, have some problems with demagnetization as the geometry prevents the PMs from being made long enough (along the magnetization) to protect them against demagnetization. Especially for low remanence materials where a larger volume of PM material is used, self-demagnetization can be an issue if the length is constrained to be small compared to the cross section. The surface mounted PM gives higher torque than the other types for high remanence materials that have good demagnetization resistance. For low demagnetization resistance the capped PM rotor gives more torque for high remanence materials.

From the above it can be concluded that demagnetization resistance of the PM material is more important than a high remanence in electrical machine design. With this in mind it can be argued that a low cost PM material with fair demagnetization resistance and slightly higher remanence than ferrite PMs can be highly useful in PMSG applications.

From the stability analysis of the results in the rotor topology and PM material study, it is concluded that the air gap length, pole pitch, and the total PM energy are the most critical to the qualitative outcome. The total PM energy is the product of the volume of PM material and the maximum energy product $|BH|_{\max}$ of the material. It is noted that the air gap length relative to the size of the rest of the cross section geometry is not likely to change enough to cause significant, qualitative changes in the results. It is also noted that if the cross section is to remain geometrically similar when the pole pitch is increased, the volume of PM material should change as the square of the pole pitch. The impact of changing the total PM energy, and that of changing the pole pitch are such that they approximately cancel each other, if geometric similarity is preserved. It is therefore concluded that the results should have at least some generality.

7. Future Work

The mechanical design of the rotor in Paper I could be evaluated and the experiences used to iterate a better design. Improvements of the design could be made both with regard to electromagnetic performance, material usage, and cost of manufacture.

Development of better tools and concepts to quantify the sensitivity of calculations to uncertainty in input parameters is another possible future work. For instance the impact of errors in the models of non-linear magnetic materials, inhomogeneity of materials, and contour tolerances of stator iron uncertainties which require many parameters to describe. It would be useful to have easily accessible tools to put numbers on these uncertainties.

The behavior of the magnetic end leakage flux noted in Paper V could be used to develop models to improve the accuracy of 2D FEM in the modeling of spoke type rotors. One possibility to investigate is to add a divergence term to $\boldsymbol{B}$ in the 2D approximation to represent the axial leakage. This divergence term would be decided from the reluctance of the flux path between two poles in the end region and the difference in scalar potential between the two poles. Possibilities for determining the reluctance are either a 3D magnetic scalar potential FEM simulation of the end region, or an analytical series expansion of a solution for the magnetic scalar potential derived using separation of variables.

The PM material properties and rotor topology study made in Paper IV could be expanded in a number of ways. The capped PM rotor and spoke type rotor could be given more degrees of freedom in the optimization in order to also optimize the shape of the magnetically soft parts of the rotor. Other figures of merit could also be investigated, these could include amount of active material, or some factor for mechanical complexity. A more complex demagnetization model could also be employed to better capture the impact of demagnetization sensitivity. This might lead, however, to the need for a larger set of PM material parameters. It could also be of interest to study other types of machines. If e.g. motors were to be studied it might be advisable to add a thermal model in order to capture temperature dependence of the PM material properties.

8. Summary of Papers

Paper I

A Complete Design of a Rare Earth Metal-Free Permanent Magnet Generator

A design for a ferrite PM replacement rotor for a 12 kW PMSG originally using an NdFeB PM rotor is described. A complete mechanical and electromagnetic design is presented. The new rotor will give similar electrical properties as the original rotor; losses will be slightly higher and output voltage slightly lower. Mechanically the rotor is much heavier; but it also has a larger moment of inertia, which could be beneficial from a control perspective.

The author did the majority of the work.

Published in Machines, 2014.

Paper II

Air Gap Magnetic Flux Density Variations due to Manufacturing Tolerances in a Permanent Magnet Synchronous Generator

The impact of manufacturing tolerances on the magnetic flux density in the air gap is investigated and both magnetic and mechanical tolerances are considered. The investigation is done on a machine built according to the design presented in Paper I . It is found that the air gap magnetic flux density is significantly lower than expected. The probable cause is that the PMs have lower remanence than specified.

The author did the majority of the work.

Presented as a poster at the XXIInd International Conference on Electrical Machines, Lausanne, Switzerland, September 2016.

Paper III

Winding Design Independent Calculation Method for Short Circuit Currents in Permanent Magnet Synchronous Machines

A method for calculating the short circuit current without a fixed winding design is proposed. The method is based on the two-reaction theory of synchronous machines proposed by Park in 1929. The electric circuit parameters are replaced by magnetic circuit equivalents, which allows the differential

equations describing the transient behavior of a synchronous machine to be used with only knowledge of the space occupied by the winding and the winding conductivity. A method for how to calculate the magnetic circuit equivalent parameters is also given. The method is validated against transient finite element method simulations on two different machine designs and in a total of three different cases. The validation shows reasonable agreement between the proposed method and the transient finite element method simulations.

The author did the majority of the work.

Presented as a poster at the XXIIIrd International Conference on Electrical Machines, Alexandroupoli, Greece, September 2018.

Paper IV

The influence of permanent magnet material properties on generator rotor design

A method to investigate how different kinds of permanent magnet (PM) materials alter the performance of different PM rotor topologies is developed and demonstrated. The PM materials are described by their remanence, recoil permeability and a parameter for the demagnetization resistance. The rotor topologies are: surface mounted PM rotor, spoke type PM rotor and capped PM rotor. For each point in the PM material space, each topology is optimized for maximum torque under resistive load and a fixed stator current for a fixed amount of PM magnetic energy. The maximum torque obtained without risking demagnetization of the PMs in the rotor is then used as figure of merit in the comparison between rotor topologies. It is found that the spoke type PM rotor is the best option for low remanence PM materials. Further it is found that the surface mounted PM rotor is the best option for high remanence PM materials if they have sufficient demagnetization resistance, otherwise the capped PM rotor is a better option.

The author did the majority of the work.

Submitted to IET Electric Power Applications on 2 May 2018.

Paper V

Experimental Evaluation of a Rare Earth-Free Permanent Magnet Generator

The generator from Paper I and Paper II is experimentally evaluated in no load and load tests. The two dimensional design simulations made for Paper I are updated with the mean air gap length and mean permanent magnet remanence reported in Paper II to validate the simulations. Comparison is made by comparing terminal voltages and line currents for the different test cases. The magnetic end leakage flux is investigated as a possible cause of the discrep-

ancy between simulation and experimental results. The investigation is done by using three dimensional finite element method simulations. The three dimensional simulations are also validated with measurements of the magnetic flux density in the end regions. It is concluded that the magnetic end leakage flux is a likely explanation for the discrepancy between the design simulations and the experimental result.

The author had major involvement in all parts of the work. The simulations and measurements of the magnetic end leakage flux, and the frequency analysis of the no load voltage were done in collaboration with J. Sjölund and M. Berg, respectively.

Submitted to IEEE Transactions on Energy Conversion on 11 October 2018.

Paper VI

Development of Power Electronics Based Test Platform for Characterization and Testing of Magnetocaloric Materials

A method of characterizing magnetocaloric materials is proposed. The method is based on hybrid excitation where both a permanent magnet and an electromagnet are used together to create a pulsating magnetic flux density in the air gap of a three legged iron core. To get frequencies appropriate for experiments on magnetocaloric materials, the electromagnet is powered by a custom built single phase H-bridge inverter. A scaled down prototype is built, tested, and found to work as expected. It is concluded that the method is adequate and that a full scale iron core should be made.

The author was involved in the magnetic simulation and design of the iron core.

Published in Advances in Electrical Engineering, 2015.

Paper VII

Determining demagnetisation risk for two PM wind power generators with different PM material and identical stators

The risk of demagnetization in two permanent magnet synchronous generators with identical stators is studied. One has the spoke type rotor from Paper I and the other has the surface mounted neodymium-iron-boron permanent magnet rotor the spoke type rotor was designed to replace. The generators are simulated during several short circuit events with permanent magnet properties for different temperatures. Both machines are found to be able to sustain the short

circuits without significant demagnetization at normal operating temperatures, while there is significant demagnetization at extreme temperatures.

The author designed the ferrite permanent magnet rotor used in one of the studied machines.

Published in IET Electric Power Applications, 2016.

Paper VIII

Magnetic End Leakage Flux in a Spoke Type Rotor Permanent Magnet Synchronous Generator

The magnetic end leakage flux in a spoke type rotor is investigated by both simulations and measurements on the generator from Paper I , Paper II , and Paper V. Good agreement between the simulations and measurements are found. About a fifth of the magnetic flux from the PM is found to pass between poles in the end region for the investigated generator. Curve fitting is used in an attempt to quantify the behavior of the end leakage flux with respect to stator diameter, PM size, machine length and number of poles. An empirical expression for the ratio of the magnetic flux through the stator computed by 3D simulations and that computed by 2D simulations is proposed.

The author designed and performed the measurements, collaborated on the simulations with J. Sjölund, did the curve fitting and wrote most of the text.

Intended for presentation at the 19th International Conference on Electrical Machines and Drives, Madrid, Spain, March 2017. Presentation was canceled when it was discovered that the conference program was of poor quality.

9. Svensk sammanfattning

Elektricitet kan genereras på olika sätt men vanligast är att en roterande elektrisk maskin av typen synkrongenerator används. I en synkrongenerator snurrar en magnet omgiven av ledare i vilka den elektriska spänning som alstras av det växlande magnetfältet kan driva en ström i. Magneten i synkronmaskinen kan antingen vara en elektromagnet eller en permanentmagnet (PM).

Sedan ungefär mitten av 1980-talet har permanentmagneter gjorda av metallerna neodym, järn och bor (NdFeB) varit populära då de haft bra prestanda i förhållande till pris. Under 2011 ändrades dock detta och världsmarknadspriset på neodym plötsligt gick upp med ungefär en faktor tio när Kina, som står för merparten av världsproduktionen, införde exportrestriktioner. För att möta den osäkerhet i tillgång och pris på NdFeB-magneter som uppdagades i och med detta, samt minska miljöpåverkan vid utvinning av råmaterial för NdFeB-magneter, har det startats forskning på dels nya PM-material och dels på att bättre använda andra existerande PM-material istället för NdFeB-magneter. Den här avhandlingen beskriver försök att konstruera permanentmagnetiserade synkronmaskiner (PMSM:er) utan att använda NdFeB-magneter. Två olika angreppsätt används: dels att använda ferritmagneter istället för NdFeB-magneter och dels att studera vilka egenskaper nya PM-material behöver för att vara användbara till PMSM:er.

För att undersöka möjligheterna att ersätta NdFeB-magneter med ferritmagneter konstruerades och byggdes en ny rotor till en PMSM som ursprungligen byggts med en rotor med ytmonterade NdFeB-magneter. I en rotor med ytmonterade permanentmagneter sitter magneterna på en magnetiskt ledande ring av järn eller stål och är magnetiserade radiellt. Den nya rotorn har permanentmagneter placerade mellan poler av magnetiskt ledande stål som samlar ihop det magnetiska flödet från magneten och leder ut det i luftgapet. I den typen av rotor är magneterna tangentiellt magnetiserade. Då magneterna sitter som ekrarna i ett hjul kallas den för ”ekerrotor”. Ekerrotorns konstruktion gör att en högre magnetisk flödestäthet i maskinens luftgap kan erhållas jämfört med vad som kan erhållas i en ytmonterad PM-rotor som använder samma PM-material. Dock till priset av en mekaniskt mer komplex rotor. Trots denna lösning förväntades den nya rotorn ge lite lägre spänning än den ursprungliga. Statorn var dock överdimensionerad så att samma uteffekt skulle kunna erhållas genom att dra en större ström. Den nya rotorn skulle även bli mycket tyngre men därmed även få ett större tröghetsmoment, det senare kan vara av nytta när generatorn ska styras.

Efter att den nya rotorn byggts undersöktes prestandan på den generator den satt i. En första undersökning mätte den magnetiska flödestätheten i luftgapet

mellan stator och rotor, storleken på magneterna, magneternas styrka och hur långt avståndet mellan rotorn och statorn, luftgapslängden, var. Det framkom att den magnetiska flödestätheten i luftgapet var lägre än beräknat i konstruktionsunderlaget och att detta till stor del berodde på att magneterna som använts inte var så starka som tillverkaren utlovat. Senare mätningar visade att konstruktionssimuleringarna inte stämde även när den uppmätta styrkan på magneter och luftgapslängden användes. För att försöka förklara skillnaden undersöktes det magnetiska flödet runt ändarna på maskinen. Undersökningen gjordes genom tredimensionella simuleringar och mätningar för att verifiera dessa. Det framkom att det läckage av magnetiskt flöde som förekom runt ändarna på generatorn till stor del kan förklara skillnaderna mellan beräknad och uppmätt spänning.

Slutsatsen från undersökningen av möjligheterna att ersätta NdFeB-magneter med ferritmagneter blev att det är möjligt. Det framkom även att det är av vikt att de använda materialen har utlovade egenskaper, samt att den typ av rotor som behövs för att ferritmagneter ska gå att använda behöver modelleras så att det magnetiska flödet i maskinändarna tas med i beräkningarna.

Undersökningen av vilka egenskaper som gör ett PM-material användbart i en PMSG gjordes genom att tre olika rotortyper optimerades för olika PM-materialegenskaper. För att beskriva PM-materialets egenskaper användes tre parametrar. Den första var remanensen som är ett mått på hur stark en magnet är och som anger den magnetiska flödestätheten i en oändligt lång eller ringformad magnet. Den andra var rekylpermeabiliteten som är ett mått på hur mycket en magnet ändrar sin magnetiska flödestäthet som svar på ett yttre magnetfält. Den sista var en parameter som angav PM-materialets motståndskraft mot avmagnetisering. De tre rotortyperna som användes var ytmonterad PM-rotor, ekerrotor och en rotor med täckta magneter. Rotorn med täckta magneter liknar den ytmonterade men har en bit magnetiskt mjukt stål mellan magneten och luftgapet. Beräkningarna gjordes i ett nät där de tre PM-materialparametrarna varierades. För varje knutpunkt i nätet genomfördes beräkningar för att optimera hur mycket vridmoment var och en av de tre rotortyperna kan åstadkomma när de driver en given ström i en resistiv last. Optimeringen skedde under villkoret att magneterna inte får avmagnetiseras vid en kortslutning. En känslighetsanalys utfördes för att undersöka hur ett antal olika maskinparametrar påverkar utfallet av studien.

Från undersökningen kan man dra slutsatsen att ekerrotorn ger mest vridmoment för PM-material med låg remanens men behöver viss motståndskraft mot avmagnetisering för att vara användbar. Vidare kan man dra slutsatsen att om motståndskraften mot avmagnetisering är god ger ytmonterad rotor högst vridmoment för material med hög remanens medan om motståndskraften är låg är rotorn med täckta magneter bättre. Från känslighetsanalysen kan man dra slutsatsen att valet av maskinparametrar inte är avgörande för utfallet.

10. Acknowledgments

The work for this thesis has been funded by the Swedish Research Council, grant number 2012-4706; ÅForsk, Ångpanneföreningen's Foundation for R&D, grant number 12-295; and Carl Trygger's foundation, grant number 15:152. Liljewalchs travel scholarship funded the author's participation in the XXIIth International Conference on Electrical Machines and the presentation of Paper II at the same conference. The above financial support is gratefully acknowledged. The work was conducted within the STandUP for Energy strategic research framework.

I would like to thank my main supervisor Dr. Sandra Eriksson for support throughout these five years. I would further like to extend my thanks to my co-supervisors Professor Mats Leijon and Dr. Marcus Berg.

All colleagues at the Division of Electricity, both past and present, also have my gratitude for company, support, and interesting discussions. A few that comes to mind are Urban: and Arne for rewarding discussion on FEM simulations of electrical machines; Olov for discussions on vector calculus mingled with electromagnetism; Morgan, Stefan, and Senad for for both work related and non-work related discussions; Mikael for frequent reminders not to work after five o'clock; and Elin and Jonathan for the company on the occasional stroll in Kronparken.

Jag vill tacka min mamma (postumt, sorgligt nog) och pappa för att ni lät mig hållas när jag ville bygga något eller mecka med saker. För att ni inte skällde (så mycket) när min klåfingriga nyfikenhet gjorde att något gick sönder eller blev smutsig. För att ni lassade på mig med verktyg och leksaker som jag fick bygga ihop själv och för att ni uppmuntrade mina försök att slöjda och hantverka. Jag vill också tacka mina fina släktingar för att ni finns där och speciellt för ert stöd i samband med att mamma dog i cancer hösten 2017.

Mina vänner, gamla som nya, ska också ha tack för att ni gör min tillvaro trevligare. Tomas, som fick mig att tänka på ingenjörsstudier; Dorothea; Mattias; brädspelsgänget Elin, Lamu, Malin, Hilde och Simon; Samuel; Johanna; Nils, vi borde ge oss på att skriva någon spexig sång igen; Dr. Bishop, för kamratskap och hjälp med engelskan; Micke och Randi; Camilla; Max och Andreas, jag hoppas på tillfälle att röja på någon konsert med er snart; Jonas; träningskamraterna i Uppsala Historiska Fäktskola (ni är för många för att räkna upp alla); Edward för alla år med nyckelharpslektioner; och alla ni som har överseende med att jag glömt nämna er vid namn.

Sist: Valdis, älskling! Du gör mig så glad! Tack för att du ställt upp och tagit på dig alla resorna som vårat distansförhållande kräver under hösten jag skrivit på avhandlingen. Din kärlek gör min tillvaro så mycket trevligare och jag hoppas att jag ger dig lika mycket tillbaka. Jag hoppas att vi får hålla av varandra resten av livet. Puss på dig!

References

[1] K.J. Binns and A. Kurdali. Permanent-magnet a.c. generators. *Proceedings of the Institution of Electrical Engineers*, 126(7):690–696, July 1979.

[2] R. Lacal-Arántegui. Materials use in electricity generators in wind turbines – state-of-the-art and future specifications. *Journal of Cleaner Production*, 87:275–283, January 2015.

[3] M. Rahman and G. Slemon. Promising applications of neodymium boron iron magnets in electrical machines. *IEEE Transactions on Magnetics*, 21(5):1712–1716, September 1985.

[4] L. Baldi, M. Peri, and D. Vandone. Clean energy industries and rare earth materials: Economic and financial issues. *Energy Policy*, 66:53–61, March 2014.

[5] P. Eklund. *Rare Earth Metal–Free Permanent Magnet Generators*. Licentiate thesis, Uppsala University, Division of Electricity, 2016.

[6] M. Doppelbauer. The invention of the electric motor. Accessed from `https://www.eti.kit.edu/english/1376.php` and `https://www.eti.kit.edu/english/1390.php` on 2016-05-05, 2014.

[7] M. Tokushichi. Magnet steel containing nickel and aluminium, January 1936. US Patent 2,027,994.

[8] R. M. Saunders and R. H. Weakley. Design of permanent-magnet alternators. *Transactions of the American Institute of Electrical Engineers*, 70(2):1578–1581, July 1951.

[9] G.E. Willem, R.G. Wolfgang, and S.A. Leopoldus. Method of making magnetically anisotropic permanent magnets, September 1956. US Patent 2,762,778.

[10] J. Braun Herman. Permanent magnet rotor, May 1958. US Patent 2,836,743.

[11] D. Das. Twenty million energy product samarium-cobalt magnet. *IEEE Transactions on Magnetics*, 5(3):214–216, September 1969.

[12] E.F. Hammond Jr., A.E. King, and A.L. Jokl. Permanent magnet generators for portable military power. Technical report, DTIC Document, 1971.

[13] J.J. Croat. High energy product rare earth-iron magnet alloys, July 1989. US Patent 4,851,058.

[14] E.K. Delczeg-Czirjak, A. Edström, M. Werwiński, J. Rusz, N.V. Skorodumova, L. Vitos, and O. Eriksson. Stabilization of the tetragonal distortion of Fe_xCo_{1-x} alloys by C impurities: A potential new permanent magnet. *Phys. Rev. B*, 89:144403, April 2014.

[15] S. Eriksson, A. Solum, M. Leijon, and H. Bernhoff. Simulations and experiments on a 12 kW direct driven PM synchronous generator. *Renewable Energy*, pages 674–681, April 2008.

[16] Fredrik Bülow. *A Generator Perspective on Vertical Axis Wind Turbines*. PhD thesis, Uppsala University, Electricity, 2013.

[17] S. Apelfröjd, S. Eriksson, and H. Bernhoff. A review of research on large scale modern vertical axis wind turbines at uppsala university. *Energies*, 9(7), July 2016.
[18] S. Sjökvist and S. Eriksson. Investigation of permanent magnet demagnetization in synchronous machines during multiple short-circuit fault conditions. *Energies*, 10(10), October 2017.
[19] S. Sjökvist, M. Rossander, and S. Eriksson. Permanent magnet working point ripple in synchronous generators. *The Journal of Engineering*, 2017:158–161(3), May 2017.
[20] S. Sjökvist and S. Eriksson. Experimental verification of a simulation model for partial demagnetization of permanent magnets. *IEEE Transactions on Magnetics*, 50(12):1–5, December 2014.
[21] S. Sjökvist and S. Eriksson. Study of demagnetization risk for a 12 kW direct driven permanent magnet synchronous generator for wind power. *Energy Science & Engineering*, 1(3):128–134, September 2013.
[22] E. Lejerskog. *Theoretical and Experimental Analysis of Operational Wave Energy Converters*. PhD thesis, Uppsala University, Electricity, 2016.
[23] B. Ekergård. *Full Scale Applications of Permanent Magnet Electromagnetic Energy Converters: From $Nd_2Fe_{14}B$ to Ferrite*. PhD thesis, Uppsala University, Electricity, 2013.
[24] T. Kamf. *Automated Production Technologies and Measurement Systems for Ferrite Magnetized Linear Generators*. PhD thesis, Uppsala University, Electricity, 2017.
[25] E. Hultman. *Robotized Production Methods for Special Electric Machines*. PhD thesis, Uppsala University, Electricity, 2018.
[26] B. Marcusson. *Magnetic Leakage Fields and End Region Eddy Current Power Losses in Synchronous Generators*. PhD thesis, Uppsala University, Electricity, 2017.
[27] J. J. Pérez-Loya. *Analysis and control of magnetic forces in synchronous machines*. PhD thesis, Uppsala University, Electricity, 2017.
[28] H. Fang, Sofia K., J. Ångström, J. Cedervall, P. Svedlindh, K. Gunnarsson, and M. Sahlberg. Directly obtained τ-phase MnAl, a high performance magnetic material for permanent magnets. *Journal of Solid State Chemistry*, 237:300–306, May 2016.
[29] D. Hedlund, J. Cedervall, A. Edström, M. Werwinski, S. Kontos, O. Eriksson, J. Rusz, P. Svedlindh, M. Sahlberg, and K. Gunnarsson. Magnetic properties of the fe_5sib_2–fe_5pb_2 system. *Physical Review B*, 96(9), September 2017.
[30] S. Kontos, H. Fang, J. Li, E. K. Delczeg-Czirjak, S. Shafeie, P. Svedlindh, M. Sahlberg, and K. Gunnarsson. Measured and calculated properties of B-doped τ-phase MnAl – a rare earth free permanent magnet. *Journal of Magnetism and Magnetic Materials*, November 2018.
[31] A. Hannalla. Analysis of transient field problems in electrical machines allowing for end leakage and external reactances. *IEEE Transactions on Magnetics*, 17(2):1240–1243, March 1981.

[32] V. Ruuskanen, J. Nerg, and J. Pyrhonen. Effect of lamination stack ends and radial cooling channels on no-load voltage and inductances of permanent-magnet synchronous machines. *IEEE Transactions on Magnetics*, 47(11):4643–4649, November 2011.

[33] O. Bŕó and K. Preis. On the use of the magnetic vector potential in the finite-element analysis of three-dimensional eddy currents. *IEEE Transactions on Magnetics*, 25(4):3145–3159, July 1989.

[34] C. Bruzzese, D. Zito, and A. Tessarolo. Finite reluctance approach: A systematic method for the construction of magnetic network-based dynamic models of electrical machines. In *2014 AEIT Annual Conference - From Research to Industry: The Need for a More Effective Technology Transfer (AEIT)*, pages 1–6, Trieste, Italy, September 2014.

[35] R. Helmer and B. Ponick. Analytical calculation of permanent-magnet synchronous machines using saturation-dependent poleform coefficients. In *XIXth International Conference on Electrical Machines*, pages 1–6, Rome, Italy, September 2010.

[36] B. Tomičić, S. Car, and Ž. Štih. An improved model of synchronous generator based on finite element method analysis. In *XXth International Conference on Electrical Machines*, pages 47–52, Marseille, France, September 2012.

[37] K. W. Klontz, T. J. E. Miller, M. I. McGilp, H. Karmaker, and P. Zhong. Short-circuit analysis of permanent-magnet generators. *IEEE Transactions on Industry Applications*, 47(4):1670–1680, July 2011.

[38] Z. Sun, J. Wang, D. Howe, and G. Jewell. Analytical prediction of the short-circuit current in fault-tolerant permanent-magnet machines. *IEEE Transactions on Industrial Electronics*, 55(12):4210–4217, December 2008.

[39] E. Dlala, J. Saitz, and A. Arkkio. Hysteresis modeling based on symmetric minor loops. *IEEE Transactions on Magnetics*, 41(8):2343–2348, August 2005.

[40] S. Ruoho, E. Dlala, and A. Arkkio. Comparison of demagnetization models for finite-element analysis of permanent-magnet synchronous machines. *IEEE Transactions on Magnetics*, 43(11):3964–3968, November 2007.

[41] C. Jungreuthmayer, T. Bauml, O. Winter, M. Ganchev, H. Kapeller, A. Haumer, and C. Kral. A detailed heat and fluid flow analysis of an internal permanent magnet synchronous machine by means of computational fluid dynamics. *IEEE Transactions on Industrial Electronics*, 59(12):4568–4578, December 2012.

[42] A. Kallaste, T. Vaimann, and A. Belahcen. Possible manufacturing tolerance faults in design and construction of low speed slotless permanent magnet generator. In *16th European Conference on Power Electronics and Applications (EPE'14-ECCE Europe)*, pages 1–10, Lappeenranta, Finland, August 2014.

[43] A. Kallaste, A. Belahcen, and T. Vaimann. Effect of PM parameters variability on the operation quantities of a wind generator. In *IEEE Workshop on Electrical Machines Design, Control and Diagnosis (WEMDCD)*, pages 242–247, Torino, Italy, March 2015.

[44] G. Heins, T. Brown, and M. Thiele. Statistical analysis of the effect of magnet placement on cogging torque in fractional pitch permanent magnet motors. *IEEE Transactions on Magnetics*, 47(8):2142–2148, August 2011.

[45] L. Gasparin, A. Cernigoj, S. Markic, and R. Fiser. Additional cogging torque components in permanent-magnet motors due to manufacturing imperfections. *IEEE Transactions on Magnetics*, 45(3):1210–1213, March 2009.

[46] I. Coenen, M. van der Giet, and K. Hameyer. Manufacturing tolerances: Estimation and prediction of cogging torque influenced by magnetization faults. *IEEE Transactions on Magnetics*, 48(5):1932–1936, May 2012.

[47] Z.Q. Zhu, Z. Azar, and G. Ombach. Influence of additional air gaps between stator segments on cogging torque of permanent-magnet machines having modular stators. *IEEE Transactions on Magnetics*, 48(6):2049–2055, June 2012.

[48] P. Kasinathan, A. Grauers, and E. S. Hamdi. Force density limits in low-speed permanent-magnet machines due to saturation. *IEEE Transactions on Energy Conversion*, 20(1):37–44, March 2005.

[49] G. Shrestha, H. Polinder, and J. A. Ferreira. Scaling laws for direct drive generators in wind turbines. In *2009 IEEE International Electric Machines and Drives Conference*, pages 797–803, Miami, Florida USA, May 2009.

[50] M. Barcaro and N. Bianchi. Interior PM machines using ferrite to replace rare-earth surface PM machines. *IEEE Transactions on Industry Applications*, 50(2):979–985, March 2014.

[51] T. M. Jahns and W. L. Soong. Pulsating torque minimization techniques for permanent magnet AC motor drives-a review. *IEEE Transactions on Industrial Electronics*, 43(2):321–330, April 1996.

[52] A. Wang, Y. Jia, and W. L. Soong. Comparison of five topologies for an interior permanent-magnet machine for a hybrid electric vehicle. *IEEE Transactions on Magnetics*, 47(10):3606–3609, October 2011.

[53] D. G. Dorrell, M. Hsieh, and A. M. Knight. Alternative rotor designs for high performance brushless permanent magnet machines for hybrid electric vehicles. *IEEE Transactions on Magnetics*, 48(2):835–838, February 2012.

[54] S. Eriksson and H. Bernhoff. Rotor design for PM generators reflecting the unstable neodymium price. In *XXth International Conference on Electrical Machines*, pages 1419–1423, Marseille, France, September 2012.

[55] K. Kim, D. Koo, and J. Lee. The study on the overhang coefficient for permanent magnet machine by experimental design method. *IEEE Transactions on Magnetics*, 43(6):2483–2485, June 2007.

[56] K.-C. Kim and J. Lee. The dynamic analysis of a spoke-type permanent magnet generator with large overhang. *IEEE Transactions on Magnetics*, 41(10):3805–3807, October 2005.

[57] V. Ostovic. Memory motors. *IEEE Industry Applications Magazine*, 9(1):52–61, January 2003.

[58] T. Sun, S. Kwon, J. Lee, and J. Hong. Investigation and comparison of system efficiency on the PMSM considering Nd-Fe-B magnet and ferrite magnet. In *INTELEC 2009 - 31st International Telecommunications Energy Conference*, pages 1–6, Incheon, South Korea, October 2009.

[59] G. Friedrich. Experimental comparison between wound rotor and permanent magnet synchronous machine for integrated starter generator applications. In *2010 IEEE Energy Conversion Congress and Exposition*, pages 1731–1736, Atlanta, GA, USA, September 2010.

[60] J. Kolehmainen. Optimal dovetail permanent magnet rotor solutions for various pole numbers. *IEEE Transactions on Industrial Electronics*, 57(1):70–77, January 2010.

[61] K. J. Binns and T. S. Low. Performance and application of multistacked imbricated permanent magnet generators. *IEE Proceedings B - Electric Power Applications*, 130(6):407–414, November 1983.

[62] E. Spooner and A. C. Williamson. Direct coupled, permanent magnet generators for wind turbine applications. *IEE Proceedings - Electric Power Applications*, 143(1):1–8, January 1996.

[63] A. Zavvos, A. Mcdonald, and M. Mueller. Optimisation tools for large permanent magnet generators for direct drive wind turbines. *IET Renewable Power Generation*, 7(2):163–171, March 2013.

[64] R. Pena, J. C. Clare, and G. M. Asher. Doubly fed induction generator using back-to-back pwm converters and its application to variable-speed wind-energy generation. *IEE Proceedings - Electric Power Applications*, 143(3):231–241, May 1996.

[65] P. Lampola and J. Perho. Electromagnetic analysis of a low-speed permanent-magnet wind generator. In *International Conference on Opportunities and Advances in International Electric Power Generation (Conf. Publ. No. 419)*, pages 55–58, Durham, UK, March 1996.

[66] S. Jang, H. Seo, Y. Park, H. Park, and J. Choi. Design and electromagnetic field characteristic analysis of 1.5 kW small scale wind power generator for substitution of Nd-Fe-B to ferrite permanent magnet. *IEEE Transactions on Magnetics*, 48(11):2933–2936, November 2012.

[67] M. V. Cistelecan, M. Popescu, and M. Popescu. Study of the number of slots/pole combinations for low speed permanent magnet synchronous generators. In *IEEE International Electric Machines & Drives Conference*, volume 2, pages 1616–1620, Antalya, Turkey, May 2007.

[68] W. Wu, V. S. Ramsden, T. Crawford, and G. Hill. A low speed, high-torque, direct-drive permanent magnet generator for wind turbines. In *Conference Record of the 2000 IEEE Industry Applications Conference. Thirty-Fifth IAS Annual Meeting and World Conference on Industrial Applications of Electrical Energy (Cat. No.00CH37129)*, volume 1, pages 147–154 vol.1, Rome, Italy, October 2000.

[69] Z. Chen and E. Spooner. A modular, permanent-magnet generator for variable speed wind turbines. In *Seventh International Conference on Electrical Machines and Drives (Conf. Publ. No. 412)*, pages 453–457, Durham, UK, September 1995.

[70] E. Muljadi, C. P. Butterfield, and Yih-Huie Wan. Axial-flux modular permanent-magnet generator with a toroidal winding for wind-turbine applications. *IEEE Transactions on Industry Applications*, 35(4):831–836, July 1999.

[71] J. Pyrhönen, T. Jokinen, and V. Hrabovocová. *Design of Rotating Electrical Machines*. John Wiley & Sons, second edition, 2014.

[72] J.D. Jackson. *Classical Electrodynamics*, pages 190–194. John Wiley & Sons, Inc., 1962.

[73] B.D. Cullity and C.D. Graham. *Introduction to Magnetic Materials*. Wiley-IEEE Press, second edition, 2008.

[74] R. H. Park. Two-reaction theory of synchronous machines generalized method of analysis-part i. *Transactions of the American Institute of Electrical Engineers*, 48(3):716–727, July 1929.

[75] M. G. Larson and F. Bengzon. *The Finite Element Method: Theory, Implementation, and Applications*. Springer Berlin Heidelberg, Berlin, Heidelberg, 2013. From SpringerLink (Online service).

[76] A. Arkkio. *Analysis of Induction Motors Based on the Numerical Solution of the Magnetic Field and Circuit Equations*. PhD thesis, Helsinki University of Technology, 1987.

[77] P. Eklund and S. Eriksson. Air gap magnetic flux density variations due to manufacturing tolerances in a permanent magnet synchronous generator. In *XXIInd International Conference on Electrical Machines*, pages 93–99, Lausanne, Switzerland, September 2016.

[78] P. Eklund and S. Eriksson. Winding design independent calculation method for short circuit currents in permanent magnet synchronous machines. In *XXIIIrd International Conference on Electrical Machines*, pages 1021–1027, Alexandroupoli, Greece, September 2018.

[79] B. Hague. The shape of pole-shoe required to produce a sinusoidal distribution of air-gap flux density. *Journal of the Institution of Electrical Engineers*, 62(335):921–929, November 1924.

[80] P. Eklund, S. Sjökvist, S. Eriksson, and M. Leijon. A complete design of a rare earth metal-free permanent magnet generator. *Machines*, 2(2):120–133, May 2014.

Acta Universitatis Upsaliensis

Digital Comprehensive Summaries of Uppsala Dissertations from the Faculty of Science and Technology 1746

Editor: The Dean of the Faculty of Science and Technology

A doctoral dissertation from the Faculty of Science and Technology, Uppsala University, is usually a summary of a number of papers. A few copies of the complete dissertation are kept at major Swedish research libraries, while the summary alone is distributed internationally through the series Digital Comprehensive Summaries of Uppsala Dissertations from the Faculty of Science and Technology. (Prior to January, 2005, the series was published under the title "Comprehensive Summaries of Uppsala Dissertations from the Faculty of Science and Technology".)

Distribution: publications.uu.se
urn:nbn:se:uu:diva-366344

ACTA
UNIVERSITATIS
UPSALIENSIS
UPPSALA
2018